Front. Optoelectron. 2015, 8(4): 351–378
DOI 10.1007/s12200-015-0481-3

REVIEW ARTICLE

Laser-based micro/nanofabrication in one, two and three dimensions

Wei XIONG[1], Yunshen ZHOU[1], Wenjia HOU[1], Lijia JIANG[1], Masoud MAHJOURI-SAMANI[1], Jongbok PARK[1], Xiangnan HE[1], Yang GAO[1], Lisha FAN[1], Tommaso BALDACCHINI[2], Jean-Francois SILVAIN[3], Yongfeng LU (✉)[1]

1 Department of Electrical Engineering, University of Nebraska-Lincoln, Lincoln NE 68588, USA
2 Technology and Applications Center, Newport Corporation, Irvine, CA 92606, USA
3 Institute of Chemistry of Condensed Matter of Bordeaux, ICMCB-CNRS 87, Avenue du Docteur Albert Schweitzer F-33608 Pessac Cedex, France

Abstract Advanced micro/nanofabrication of functional materials and structures with various dimensions represents a key research topic in modern nanoscience and technology and becomes critically important for numerous emerging technologies such as nanoelectronics, nanophotonics and micro/nanoelectromechanical systems. This review systematically explores the non-conventional material processing approaches in fabricating nanomaterials and micro/nanostructures of various dimensions which are challenging to be fabricated via conventional approaches. Research efforts are focused on laser-based techniques for the growth and fabrication of one-dimensional (1D), two-dimensional (2D) and three-dimensional (3D) nanomaterials and micro/nanostructures. The following research topics are covered, including: 1) laser-assisted chemical vapor deposition (CVD) for highly efficient growth and integration of 1D nanomaterial of carbon nanotubes (CNTs), 2) laser direct writing (LDW) of graphene ribbons under ambient conditions, and 3) LDW of 3D micro/nanostructures via additive and subtractive processes. Comparing with the conventional fabrication methods, the laser-based methods exhibit several unique advantages in the micro/nanofabrication of advanced functional materials and structures. For the 1D CNT growth, the laser-assisted CVD process can realize both rapid material synthesis and tight control of growth location and orientation of CNTs due to the highly intense energy delivery and laser-induced optical near-field effects. For the 2D graphene synthesis and patterning, room-temperature and open-air fabrication of large-scale graphene patterns on dielectric surface has been successfully realized by a LDW process. For the 3D micro/nanofabrication, the combination of additive two-photon polymerization (TPP) and subtractive multi-photon ablation (MPA) processes enables the fabrication of arbitrary complex 3D micro/nanostructures which are challenging for conventional fabrication methods. Considering the numerous unique advantages of laser-based techniques, the laser-based micro/nanofabrication is expected to play a more and more important role in the fabrication of advanced functional micro/nano-devices.

Keywords micro/nanofabrication, laser material interaction, carbon nanotubes (CNTs), graphene, two-photon polymerization (TPP), multi-photon ablation (MPA)

1 Introduction

Micro/nanofabrication of functional nanomaterials and micro/nanostructures remains a key research topic in nanotechnology since it is requisite in developing future functional devices, which will have significance impact on the human society [1–3]. A wide range of practical applications including micro/nanoelectronics [4–6], nano-optics [7–10], solar cells [11,12] and micro/nanoelectromechanical systems (MEMS/NEMS) [13,14] are proposed and currently being developed globally based on the advanced nanomaterials and micro/nanostructures, such as one-dimensional (1D) carbon nanotube (CNT) [15], two-dimensional (2D) graphene [16–18], and three-dimensional (3D) micro/nanostructures [19,20]. Although extensive research efforts have been invested and significant progress has been made, the growth and fabrication of such 1D, 2D and 3D nanomaterials and micro/nanostructures still face tremendous challenges to be addressed. For

Received September 16, 2014; accepted December 1, 2014

E-mail: ylu2@unl.edu

example, for the synthesis of 1D CNTs, a high growth temperature and long growth time are generally required using conventional chemical vapor deposition (CVD) methods [21,22], which is not energy and time-efficient for future industrial application. For the synthesis of 2D graphene, time-consuming CVD process and cumbersome graphene transfer steps are generally required in the mainstream production method [23]. Besides, additional patterning steps via pre-growth [24] or post-growth [25] lithography are usually required for the fabrication of graphene patterns. For the 3D micro/nanofabrication, conventional techniques are still limited to the 2D layer-by-layer strategies which is inefficient in fabricating arbitrary 3D micro/nanostructures [26].

To address the above challenges faced by the conventional fabrication methods such as thermal CVD, non-conventional laser-based approaches for material growth and processing methods were proposed due to its unique advantages comparing to the conventional fabrication method: 1) laser-assisted CVD have a much shorter heating and cooling cycle for the entire fabrication process [27]. Therefore, a faster growth rate of nanomaterials can be usually achieved. 2) Different from the conventional thermal-based methods requiring certain high substrate temperature to initiate the growth of nanomaterials, the laser material interaction can be tuned to achieve very high laser energy coupling efficiency so that efficient growth of nanomaterials can be achieved at a much lower substrate temperature [28]. 3) It is easy to achieve localized processing with focused laser beams [29], thus, the conventional multi-step fabrication process including material growth, lithography and liftoff processes can be achieved by a single-step laser-assisted fabrication process. 4) Laser-assisted fabrication can take advantages of its inherent and unique secondary effects of laser-material interactions such as optical near-field enhancements [30] and multi-photon absorption [26], which offers tight controllability on the growth location and orientation of nanomaterials and provides high designability and flexibility in 3D micro/nanofabrication.

In this review article, we systematically elaborate experimental demonstrations of the laser-based micro/nanofabrication approaches as developed in our laboratory, including laser-based micro/nanofabrication of 1D, 2D and 3D nanomaterials and micro/nanostructures. The following research topics will be presented: 1) laser-assisted CVD growth and integration of 1D CNT nanomaterial, 2) laser direct writing (LDW) of 2D graphene nanomaterial, and 3) laser-based fabrication of 3D polymeric micro/nanostructures.

2 Laser-assisted growth of one-dimensional material: carbon nanotubes

2.1 Existing methods and challenges in growth and integration of carbon nanotubes

CNTs, which are 1D cylindrical carbon molecules, have a rich diversity of chiral structures and remarkable properties. Enchanted by their intrinsic 1D structure and extraordinary properties, tremendous efforts have been devoted to the investigations of CNTs [31–33]. A wide spectrum of CNT-based applications has been conceived and investigated. For example, CNTs have been envisioned as one of the most promising candidates for fabricating nano-electronics, optics, and opto-electronics, etc [34,35]. Figure 1 has summarized the existing synthetic methods for growing CNTs.

Currently extensive investigations have been made in fabricating CNT-based components and devices, such as transistors, logic gates, interconnects, sensors and detectors [32–35,41]. However, successful implementation of CNT-based application is yet far from reality due to several

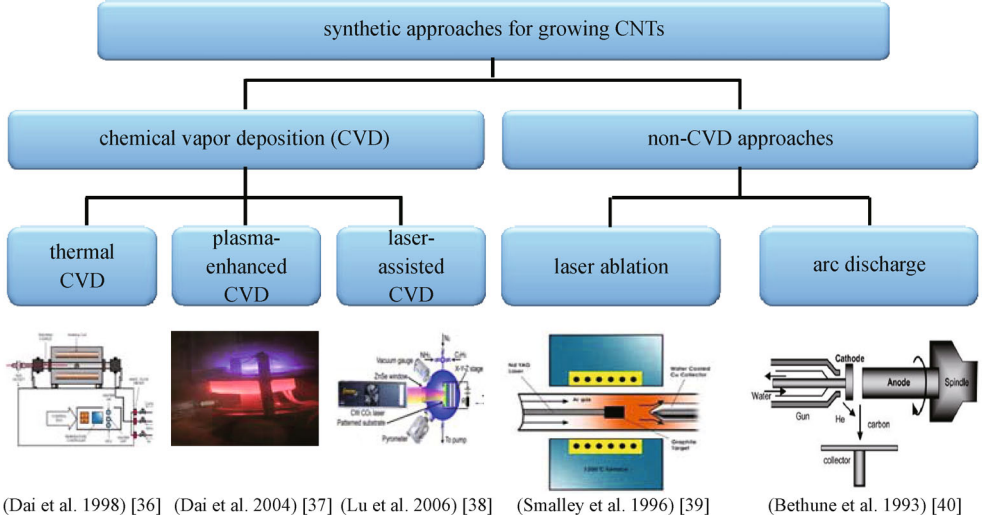

Fig. 1 Summary of the synthetic methods for growing CNTs [36–40]

critical challenges, such as the controlled growth of CNTs and the precise integration/assembly of CNTs into device structures. Ideally, it is desired that CNTs of determined electrical types were precisely wired between pre-designed electrodes with stable contacts for device fabrication [42]. However, such precise control is extremely difficult due to the ultra-tiny size of CNTs and lack of cost-efficient method for high-throughput nano-positioning of CNTs.

By far, extensive investigations have been conducted to address the challenges. There are two categories of approaches developed for assembling CNTs into device structures, as summarized in Table 1. One is the post-growth manipulation which involves manipulating CNTs using state-of-the-art nano-manipulation techniques [43,48–50]. This kind of approaches is capable of yielding CNT devices in a reliable and well controlled manner. However, it requires exquisite equipment and is intolerable time consuming, which makes it unrealistic for mass production. The other approach is *in-situ*-growth method, which involves controlled growth of CNTs on pre-defined catalyst patterns using CVD methods [38,46]. Compared with the post-growth manipulation, the *in situ* CVD growth is more economically viable for CNT integration by yielding selective and aligned CNT growth directly on various substrates. However, general CVD methods only provide coarse control in growing site and orientation. Besides, high reaction temperature for *in situ* CNT growth is another issue limiting the CNT applications in electronics and photonics. Further improvements on the precision and efficiency of CNT integration are demanded for the CNT-based device fabrication.

2.2 Laser-assisted growth of carbon nanotubes

To address above challenges, laser techniques were introduced and investigated, since lasers cannot only provide high-efficient energy sources for CNT synthesis but also have additional capability such as optical near-field effects for tight controllability on the CNT integration. In this section, a laser assisted chemical vapor deposition (LCVD) process for high-efficient CNT synthesis is introduced. Numerical simulation of the optical near-field effects as a unique property of LCVD process is presented. Based on the optical near-field effects, an optically controlled integration technique for CNT device fabrication is demonstrated. The LCVD technique can seamlessly combines the CNTs synthesis and integration in one fabrication step which only takes several minutes. Precise placement of CNTs between electrodes was achieved due to the localized heating and optical trapping effects. It is suggested that the LCVD technique is a reliable and scalable approach to achieve simultaneous CNT integration into micro/nano-architectures, which exhibits a potential for future CNT-based device fabrication.

2.2.1 Laser assisted chemical vapor deposition growth of carbon nanotubes

The LCVD technique, in general, uses lasers as the heating source for catalytic thermal decomposition of carbon species to form single-wall or multi-walled CNTs on various substrates. It has provided several unique advan-

Table 1 Current existing methods for assembling CNTs [43–47]

	post-growth methods			*in-situ*-growth methods	
method	SPM manipulation	dielectro-phoresis	tailored adhesion	E-field directed growth	flow directed growth
required sources	SPM probes	AC or DC electric field	pre-defined functionalized pattern	electrical field	flow field
assembly images		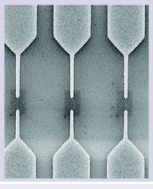	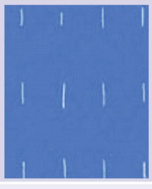	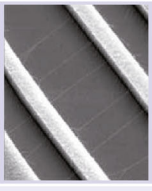	
pros & cons	precision, flexibility; assembly rate, contamination, expense	precision, assembly rate; contamination, nonflexibility	precision, assembly rate; contamination, expense	ease-of-use, low-expense; precision, temperature, nonflexibility	ease-of-use, low-expense; precision, temperature, nonflexibility
reference	Falvo et al. 1997 [43]	Krupke et al. 2007 [44]	Rao et al. 2003 [45]	Dai et al. 2001 [46]	Liu et al. 2003 [47]

tages over the conventional CVD process. To name a few, it has much shorter heating and cooling cycle for the entire CVD process [27] and possesses the capability of localized processing [29]. Furthermore, the inherent and unique secondary effects of laser-material interaction such as the optical near-field effects [30] and the resonant absorption [51] offer the LCVD further controllability on the location, orientation and even the chirality of CNTs in the CVD process.

Figure 2 shows the schematic diagram of the LCVD process for the synthesis of CNTs. Heavily doped Si wafers covered with a 2-μm-thick SiO_2 layer were used as the substrates. The electrode patterns were fabricated by conventional photolithography followed by DC sputtering. 200 nm thick ruthenium (Ru) films and 2 nm thick iron (Fe) films were deposited sequentially on the SiO_2 surface. Ru was used as the electrode material due to its low solubility with Fe, high work function, and high melting point. The Fe thin films were used as the catalyst for single-walled carbon nanotube (SWNT) growth. The SWNT growth was carried out in a LCVD chamber. A continuous-wave (CW) CO_2 laser (Synrad, firestar v40, wavelength 10.6 μm, laser beam diameter 2.5 mm ± 0.5 mm) was used to irradiate the patterned substrates. The laser power was adjusted to maintain a stable substrate temperature. Typical laser power used was ranged from 10 to 20 W. A gas mixture of acetylene (C_2H_2) and anhydrous ammonia (NH_3) with a volume ratio of 1:10 was introduced into the chamber. Anhydrous ammonia was used as a buffer gas in the LCVD process to dilute acetylene, create an etching environment to suppress the growth of amorphous carbon, and protect catalyst particles from being poisoned by amorphous carbon [16]. The reaction pressure was maintained at 10 Torr. The reaction temperature for SWNT growth was controlled around 700°C. Usually, SWNTs will grow in a vertically aligned manner if no electrical bias was applied on Ru electrodes. For growing vertically aligned SWNTs, a DC voltage was applied on electrodes to assist the aligned growth of SWNTs between electrodes. The magnitude of the DC bias varied according to the gap width, with typical values of 1–1.5 V/μm. A multi-meter was used to detect the current flow in the circuit when SWNTs bridged electrodes, which enabled *in situ* monitoring of the growth condition and detection of the end-point of the process. The reaction process was terminated immediately when a SWNT bridge structure was formed.

For the CNT characterization, a field-emission scanning electron microscope (Hitachi S4700 FE-SEM system, maximum resolution of 1.2 nm at 25 kV) was used to take scanning electron micrographs. Raman characterization of the CNTs was conducted with a Renishaw InVia Raman microscope with an excitation wavelength of 514.5 nm and a lateral resolution of about 1 μm.

Figures 3 and 4(a) show scanning electron microscope (SEM) micrographs of the vertically aligned and horizontally aligned CNTs, respectively. Highly-efficient growth of both vertically and horizontally aligned CNTs can be achieved using the LCVD process. Figure 4(b) shows a typical Raman spectrum of as-grown CNTs. A sharp radial breathing mode (RBM) peak at 204.8 cm^{-1} demonstrates the formation of the SWNTs with a diameter around 1.2 nm. The multi-SWNT bridging structures (Fig. 4(a)) could provide stable platforms for application of SWNT-based sensors. However, the SWNT growth position and orientations cannot be precisely controlled by using the parallel electrodes as shown in Fig. 4(a). Therefore, CNT growth with more precise control of growth position and orientations were further investigated in the following sections.

2.2.2 Numerical simulation of optical near-field effects

To achieve the precise control of the growth location and orientation of CNTs for future device fabrication, the optical near-field effects were investigated and exploited. It is known that ultra-sharp metallic tips can be used as optical antennae to localize and enhance optical fields

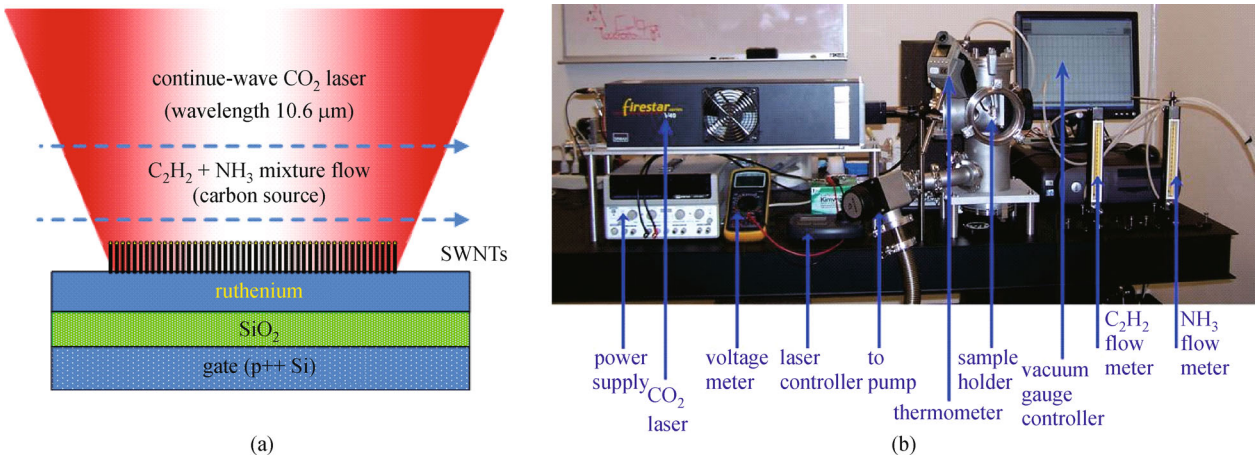

Fig. 2 (a) Schematic diagram of the LCVD process for growing CNTs; (b) photo of the home-built LCVD system

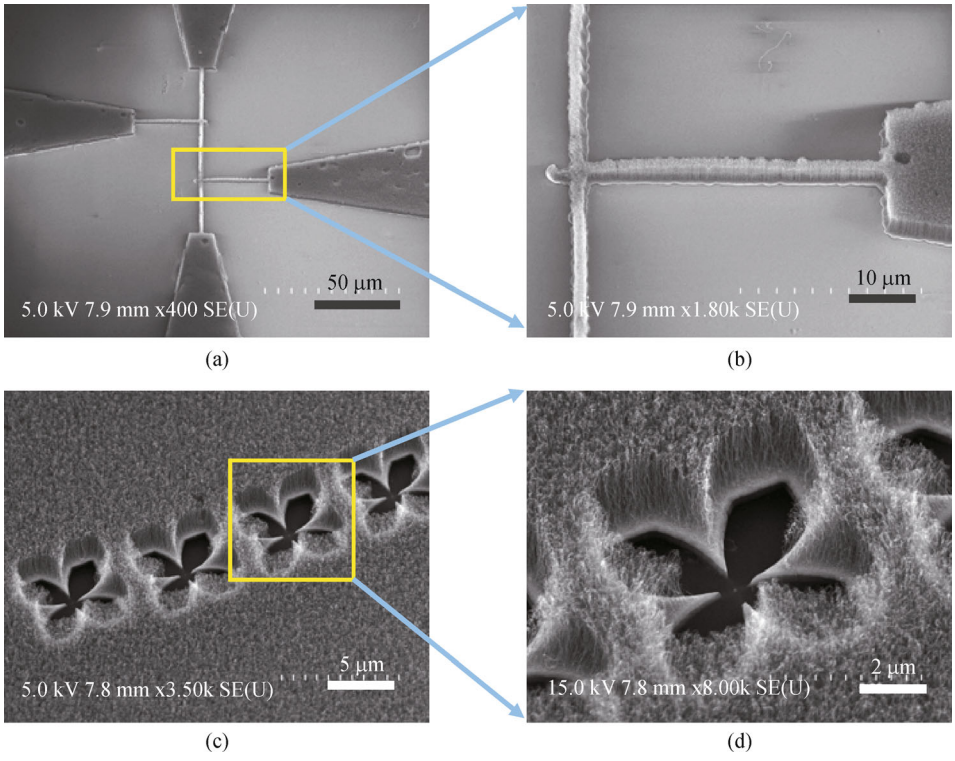

Fig. 3 Vertically aligned CNT arrays grown by the LCVD process without applying electrical bias on the Ru electrodes. Scale bar: (a) 50 μm; (b) 10 μm; (c) 5 μm; (d) 2 μm

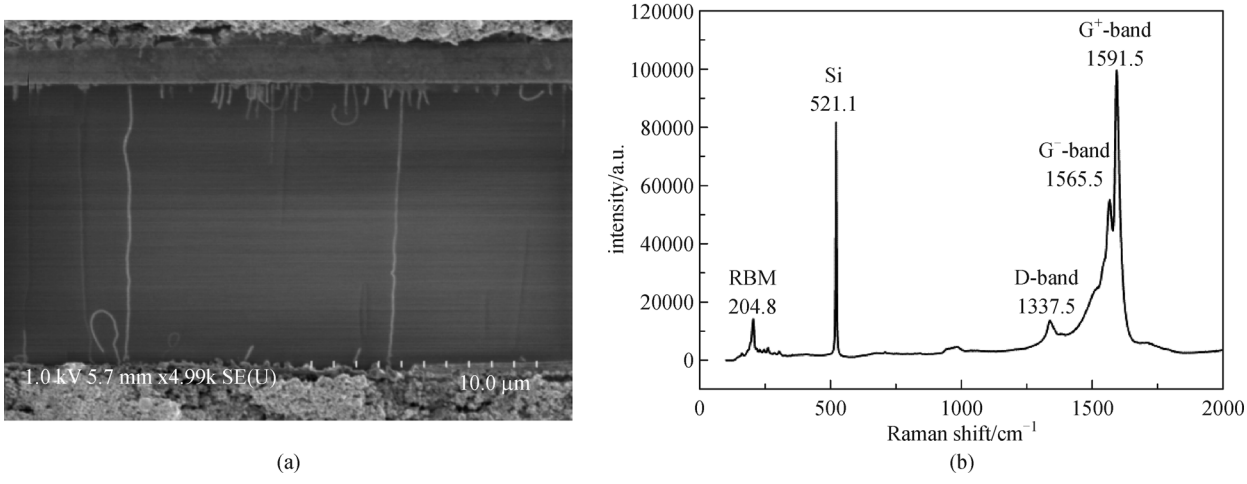

Fig. 4 (a) Horizontally aligned CNT arrays grown by the LCVD process by applying electrical bias on the Ru electrodes; (b) a typical Raman spectrum of the as-grown CNTs [52]

[53,54]. Furthermore, the enhanced optical near-field effects result in enhanced eddy-currents and localized nanoscale heating at the metallic tips. To evaluate the contribution of the optical near-field effects in the SWNT growth process, numerical simulations have been carried out using the high frequency structure simulator (HFSS, Ansoft) software package. In the simulation model, the incident laser beam was assumed to be linearly polarized and propagating perpendicularly to the substrate surface. The electromagnetic frequency was 28.3 THz, equivalent to the CO_2 laser wavelength (10.6 μm) used in the LCVD process. The gap distance between two electrode tips was assumed to be 200 nm. The tip radius was assumed to be 20 nm. Figure 5(a) shows the simulation results of the electrical field in the metallic tips. Significant electrical field enhancement can be observed at the localized tip areas, almost ten times higher than that of the rest of the electrodes. Since the electromagnetic field generates eddy

currents, the enhanced high-frequency electrical field at the tips results in significantly enhanced local eddy currents and yields an enhanced localized heating at nanometer scales. Figure 5(b) shows the heat distribution on the surface of the electrode tips. The localized heating enhancement reaches the maximum value at the tips, almost ten times higher than that of the rest of the electrodes. Therefore, a significant temperature increase at the tips is induced by the optical near-field effects. Similar simulation results have been found elsewhere [55], where the author reported that a temperature increase over three orders of magnitude could be expected in a golden tip. Since the SWNT growth strongly depends on the reaction temperature [56], an increased temperature at metallic tips will significantly promote the growth of SWNTs at the tips compared with the rest part of the electrodes, which will result in the preferential growth of SWNTs at the tips. In addition, a significant temperature increase at metallic tips also benefits the stable SWNT-metal adhesion due to the formation of carbide at high temperature, which promises stable SWNT-bridge structures.

Figure 6 shows the simulation results of electrical field and heat distribution of a multi-tip structure when it is irradiated under the linear polarized laser beams. The laser beam is normal to the substrate surface with different polarization directions, vertical (Figs. 6(a) and 6(c)) and horizontal (Figs. 6(b) and 6(d)) polarizations. As shown in Figs. 6(a) and 6(b), it is clear that the near-field enhancement reaches its maximum value at the tips whose axes are parallel to the laser polarization direction. Contrarily, there is no obvious near-field enhancement at the tips whose axes are perpendicular to the laser polarization direction. The heat distributions in Figs. 6(c) and 6(d) show the same dependency on laser polarization. It is clearly demonstrated that the near-field enhancement is highly confined and can be tuned by controlling the laser polarization, which would be of significant importance in the SWNT device fabrication.

The electric field and heat dependencies on the tip film thickness are shown in Figs. 7(a) and 7(b), respectively. Both the electric field and heat dependencies exhibit similar non-monotonic behavior. According to the numerical simulations, the maximum near-field enhancement occurs at the film thickness of 125 nm. It is well known that the optical near-field effect can be influenced by several parameters, such as the laser wavelength, tip size, and tip material. It is demonstrated that for the 10.6 μm wavelength and Ru electrode, the tip electrode reaches its structural resonance at the 125 nm film thickness for both electrical field and joule heat. Furthermore, the electrical field at the resonance status is about 2 times larger than that at non-resonance status. Hence, the localized joule heat of the tip at the resonance status is about 4 times higher than that in non-resonance status. It should be pointed out that the absolute value of the near-field enhancement may not be accurate due to the limitation of the simulation software package. However, the simulation results provide an instructive guideline for future experiments on controlled SWNT growth using the optical near-field effects. Several important parameters such as laser wavelength, tip thickness, and laser polarization should be taken into consideration and controlled in order to get maximum near-field enhancement and nanoscale heat effect for the controlled SWNT growth.

2.2.3 Parallel integration of carbon nanotubes using optical near-field effects

By making use of the tip-induced optical near-field effects in a LCVD process, a parallel integration technique was developed to achieve simultaneous integration of SWNTs into pre-designed nano-architectures at a relatively low substrate temperature, around 500°C. Figure 8 shows the illustration of the LCVD fabrication process for self-aligned CNT integration.

The SWNT-integrated structures were fabricated on p-type silicon substrates, which were covered by a 2 μm SiO_2 layer for electrical insulation. Metallic electrode patterns were fabricated following general photolithography and sputtering processes. The metallic electrodes consisted of

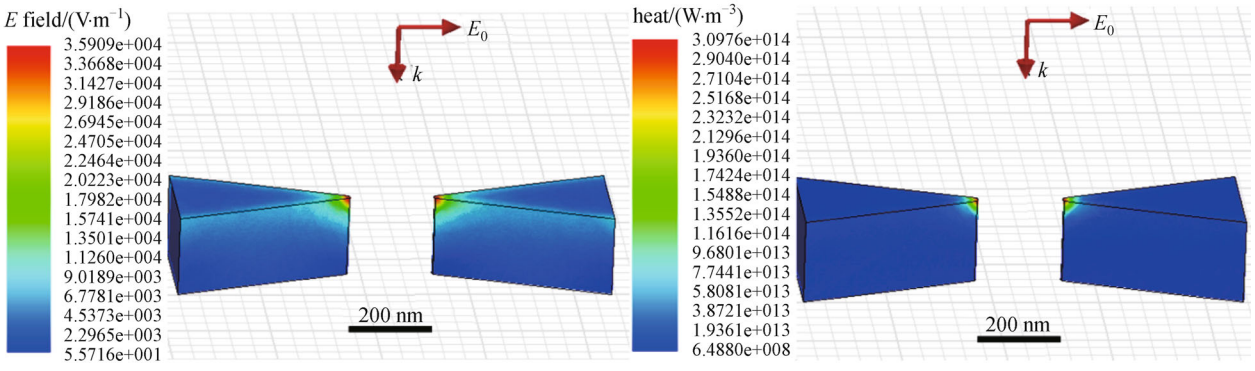

(a) (b)

Fig. 5 Numerical simulation results of (a) electrical field and (b) heat distributions around Ru tips [30]

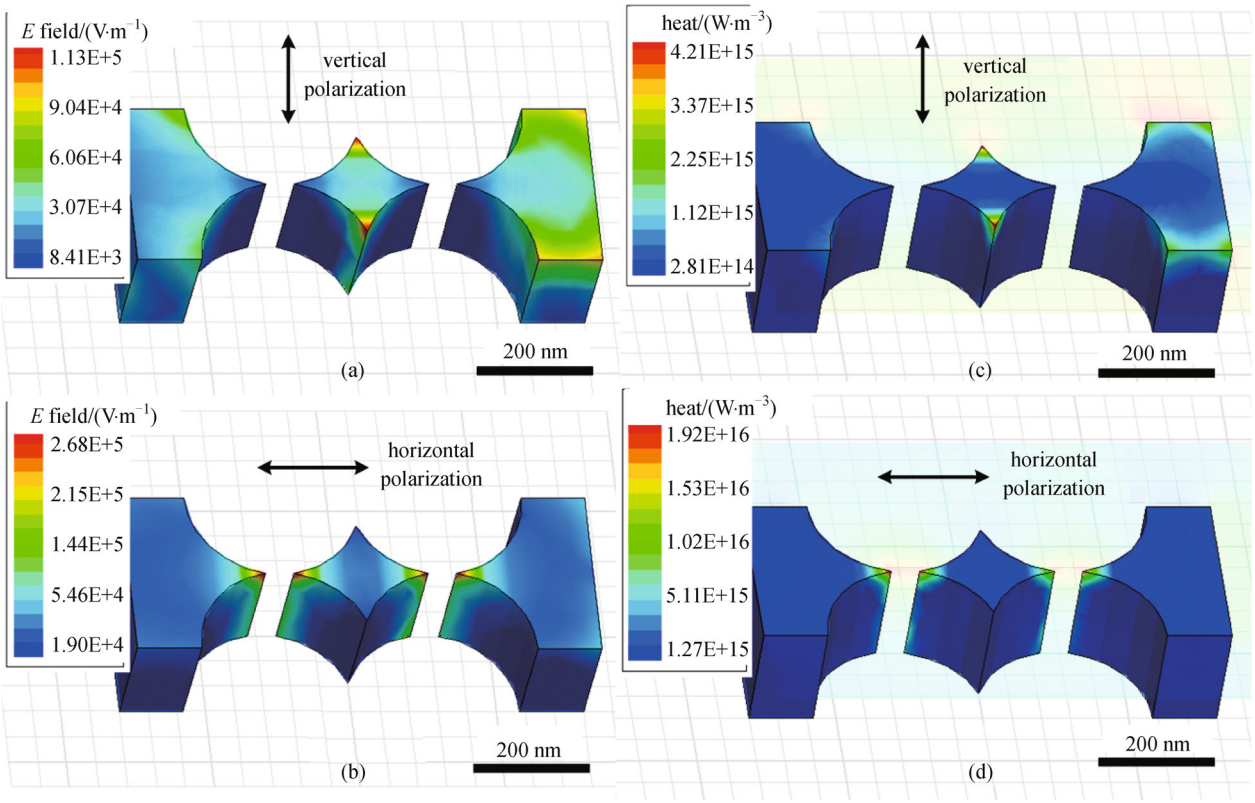

Fig. 6 Numerical simulation results of electrical field distribution in the Ru tip structure under the laser irradiation with (a) vertical and (b) horizontal *E* field polarizations; and the simulation results of heat distribution under the laser beam with (c) vertical (d) horizontal *E* field polarizations [57]

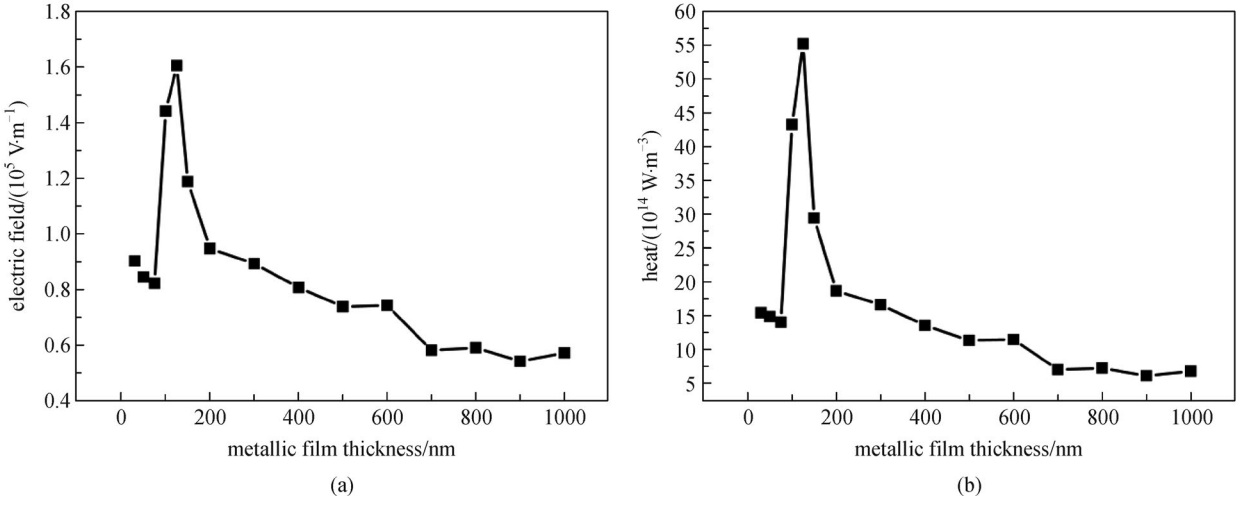

Fig. 7 HFSS simulation results demonstrating the influence of the metallic film thickness on (a) electric near field and (b) localized heating around the tip apexes, respectively [58]

multiple metallic layers, including a 200-nm ruthenium (Ru) layer, a 5-nm aluminum (Al) layer, a 1-nm iron (Fe) layer and a 20-nm Al layer sequentially from the bottom to the top. The Ru film was used as the electrode for external electrical contact. The Al/Fe/Al (5/1/20 nm) films were deposited on top of the Ru film and used as a bimetallic catalyst for growing SWNTs [59]. Ru was used for electrodes due to its high work function and high melting point. The Fe film was the active element in catalyzing the SWNT growth. The Al films were used to protect the Fe film from alloying with Ru and losing catalytic activity [59]. An extra thick Al layer, up to 20 nm, was deposited

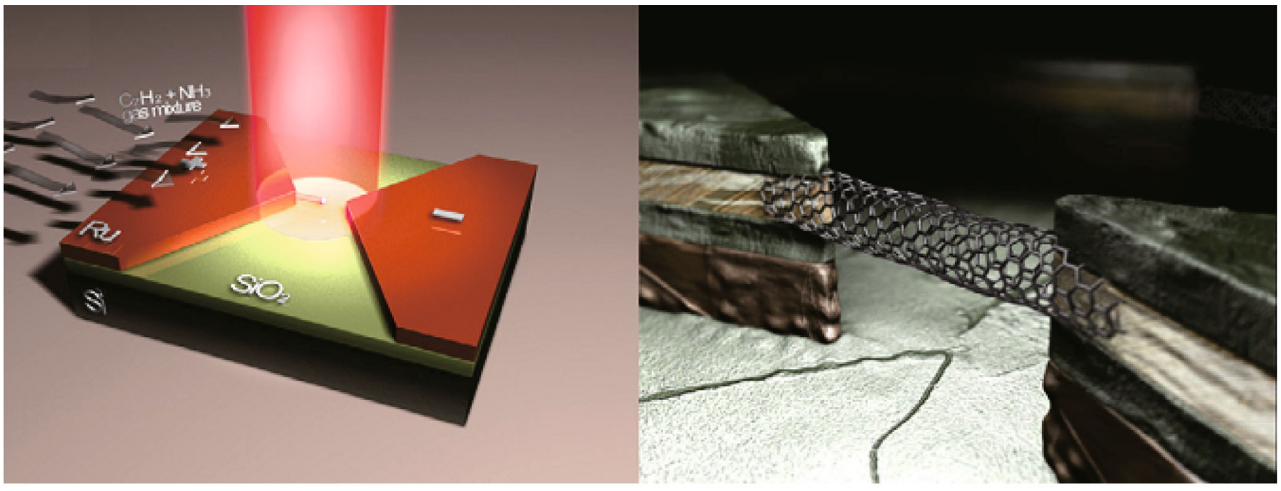

(a) (b)

Fig. 8 (a) Schematic of the LCVD fabrication process; (b) illustration of an SWNT-integrated bridge structure [57]

on top of the Fe film to protect it from being ablated during the focused-ion-beam (FIB) nano-machining process. Ultra-sharp electrode tips for growing SWNTs were fabricated by using an FEI Strata 200xp FIB system. The gap between the two electrodes was controlled to be around several hundred nanometers. Electrode patterns containing multiple pairs of tip-shaped electrodes were fabricated. Growth of SWNTs was performed through an LCVD process as shown in Fig. 8. The detailed experimental setup is the same as the conventional LCVD process as descripted in Section 2.2.1. However, the substrate temperature of the LCVD process here is only 500°C, which is 200°C lower than the conventional LCVD process due to the optical near-field heat enhancement.

Figure 9 shows the self-aligned SWNT growth with a simple electrode structure containing two pairs of parallel electrode tips as used in the LCVD process. The laser polarization was set to be parallel to the electrode tip arrangement, as shown in Fig. 9(b). Figures 9(c) and 9(d) exhibit zoomed-in images of the squared parts in Fig. 9(b) and clearly show precisely integrated SWNTs between each pair of tip-shaped electrodes. Only one SWNT was observed between each pair of the electrodes. Relatively, thick SWNT morphologies were observed in the SEM micrographs, which could be ascribed to the following reasons, including e-beam-induced carbon deposition on the tubes during SEM characterization [60], surface potential difference and charge injection between the tubes and the SiO_2 substrates induced by the electron-beam irradiation [61–63]. It is interesting to observe that the SWNTs started from the electrode tips, indicating a site-selective growth mode.

Based on the above results, more sophisticated electrode patterns containing four pairs of electrode tips were fabricated to demonstrate the feasibility of parallel SWNT integration. As shown in Fig. 10, two pairs of tip-shaped electrodes were fabricated by carving an isolated metallic island in each metallic bar. The laser polarization was set to be parallel to the arrangement of the tip arrays, as shown in Fig. 10(a). The tip-gap distance was a couple of hundred nanometers. Figures 10(b) and 10(c) show zoomed-in images of the squared regions in Fig. 10(a), and clearly show precisely integrated SWNTs between each pair of the electrodes. Growth of SWNTs was observed selectively at the electrode tips. Most of the SWNTs were precisely wired from tip to tip. Some SWNTs were observed going astray (Fig. 10(c)), which is ascribed to the distorted electric field distributions during the LCVD process.

In this study, it was found that laser polarization could significantly influence the selective growth of SWNTs which matched with the simulation results in Section 2.2.2. To experimentally investigate the influence of laser polarization, cross-shaped electrode patterns were fabricated, as shown in Fig. 11. Each cross-shaped electrode was carved into two pairs of perpendicularly arranged tips, as shown in Figs. 11(b) and 11(c). For equal comparison and easy cutting, all electrode tips were fabricated with a tip angle close to 90°. The laser polarization was set to be parallel to one pair of the tips, as shown in Fig. 11(a). To exclude the influence of electrical field, no external electrical field was applied to the electrodes. After the LCVD process, SWNTs were precisely wired between tips parallel to the laser polarization, as shown in Figs. 11(b) and 11(c). Therefore, the growth of SWNTs showed obvious selectivity on position and orientation between the electrode tips parallel to the laser polarization.

3 Laser-assisted growth of two-dimensional material: graphene

Graphene, a single sheet of graphite crystal, has drawn tremendous attentions from both academic and industrial

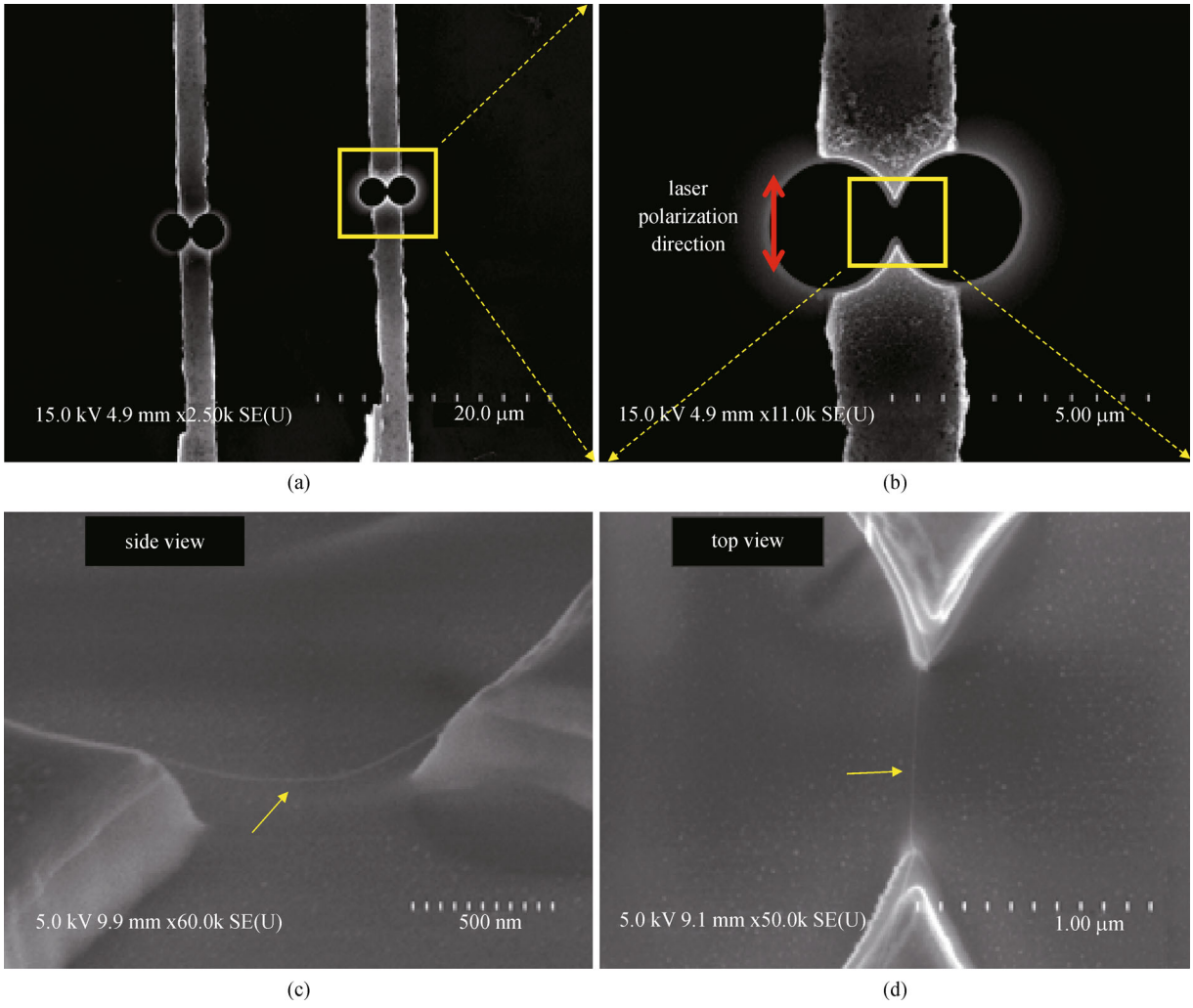

Fig. 9 (a) SEM micrograph of the electrode pattern containing two pairs of tip-shaped electrodes; (b) SEM micrograph of the zoomed-in region of the electrode tips; (c) and (d) zoomed-in SEM micrographs showing the SWNT-integrated bridge structures in a side view and top view, respectively. The arrows in (c) and (d) indicate the location of the SWNT bridge [57]

communities soon after its discovery in 2004 due to its unique and outstanding electrical [64,65], mechanical [66], thermal [67], and optical properties [68,69]. Especially, due to its ultra-high carrier mobility and wide-range optical transparency, graphene has been envisioned as one of the best candidates for future flexible and transparent electronics or optoelectronics [18], including touch screen display [23], solar cells [70,71], bio sensors [72,73], and the transparent electrodes for replacing the indium-tin oxide (ITO) films [74–77]. The nanomanufacturing of large-scale and high-quality graphene patterns on various desired substrates remains the key for the future graphene application, and it has become a hot research topic in current global competition.

3.1 Existing methods and challenges in fabricating graphene patterns

The fabrication of graphene patterns can be achieved through various different methods. Most of them follow the "synthesis + patterning" strategy [25], for example, graphene synthesis by CVD on Cu foils and then pattering through plasma etching with a shadow mask. Although high-quality graphene patterns can be reliably fabricated using the above "synthesis + patterning" approaches, the typical fabrication generally requires multiple processing steps which are very time-consuming and lack of economy-viability. Therefore, there is always a desire for searching a more cost-effective approach which can achieve the scalable fabrication of graphene patterns by less number of steps or even single step for saving the fabrication time and cost. Direct writing technique has been proposed and appeared as one of the promising approaches. Figure 12 demonstrates an illustration of fabricating graphene patterns using direct writing technique [78]. Comparing with the conventional "synthesis + patterning" approaches, the direct writing approach provides more flexibility in arbitrary graphene pattering

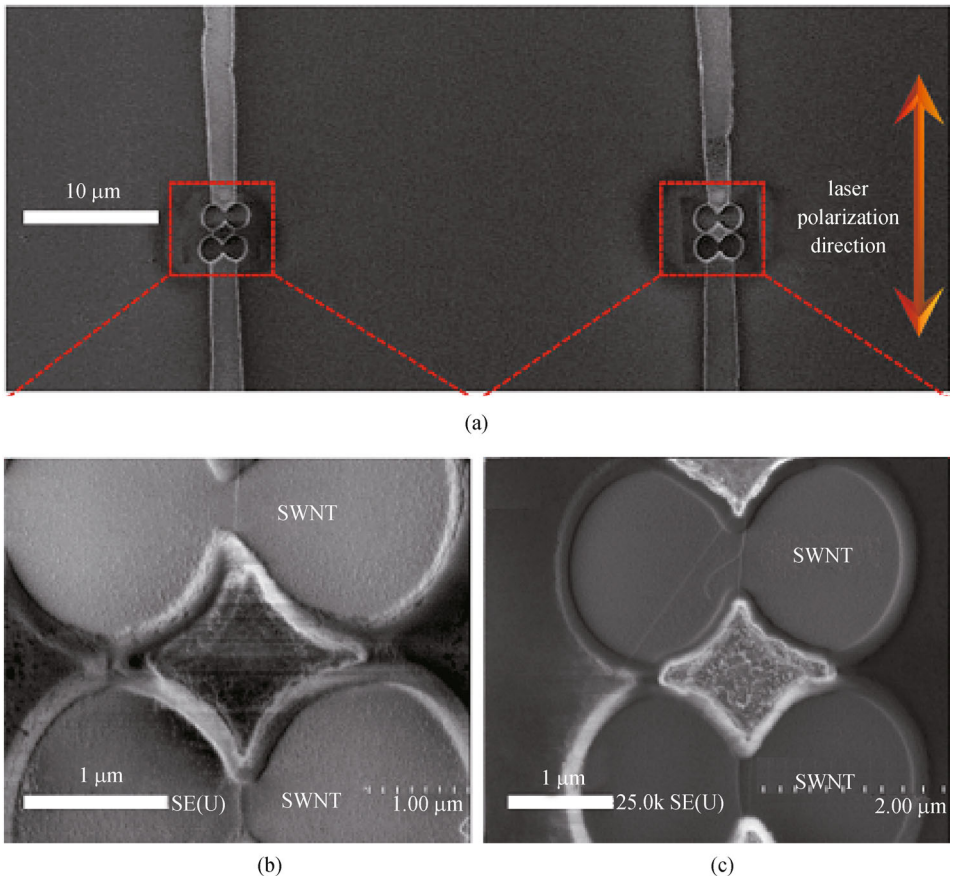

Fig. 10 (a) SEM micrograph of the electrode pattern containing four pairs of tip-shaped electrodes; (b) and (c) SEM micrographs of the square regions in (a), showing the SWNT-integrated bridge structures [57]

and requires no mask in the fabrication process which can result in reduction of the fabrication cost. More importantly, single-step fabrication of the graphene patterns can be achieved by combining the graphene growth and patterning steps together, resulting in a significant enhancement of production efficiency. Currently, there are two LDW methods available for the fabrication of graphene patterns. One is the LDW graphene patterns on graphene oxide (GO) film via localized thermal reduction [79,80], as shown in Fig. 13(a). The other is LDW graphene patterns on Ni foil via localized LCVD process [81,82], as shown in Fig. 13(b). In both methods, simultaneous graphene growth and patterning have been successfully achieved in a single-step process.

Despite of the significant progress in fabricating graphene patterns via LDW techniques, two main challenges still exist on the road toward cost-effective and large-scale nanomanufacturing of graphene patterns for practical application. First, a vacuum chamber or an airtight environment filled with inert gas such as N_2 is always required for fabrication process [80]. A much more cost-viable way of fabricating graphene patterns at ambient conditions is lacking. Second, the direct deposition of graphene patterns on desired dielectric substrates is still challenging. Post-growth graphene transfer from the synthesis substrates such as GO film or Ni foil to the application substrates such as glass substrates is still required [81,82].

3.2 Laser direct writing of graphene patterns on dielectric substrates

To addressing the challenges, we proposed and developed a novel laser-based method for direct writing arbitrary graphene patterns on insulated substrates such as glasses in open air without the use of vacuum chamber as usually required by the CVD growth of graphene. Femtosecond laser combined with a high resolution *X*-*Y* piezo-stage was used to write complex graphene patterns on nickel/carbon/ substrates. After the laser writing process, the remaining Ni top-layer can be simply removed through chemical etching process leaving only the as-written graphene patterns on the glass substrates. The new fabrication method can get rid of the expensive and relatively slow thermal CVD process in a vacuum chamber and achieves room-temperature fabrication of the graphene patterns directly on the insulated substrates without any additional graphene transfer process.

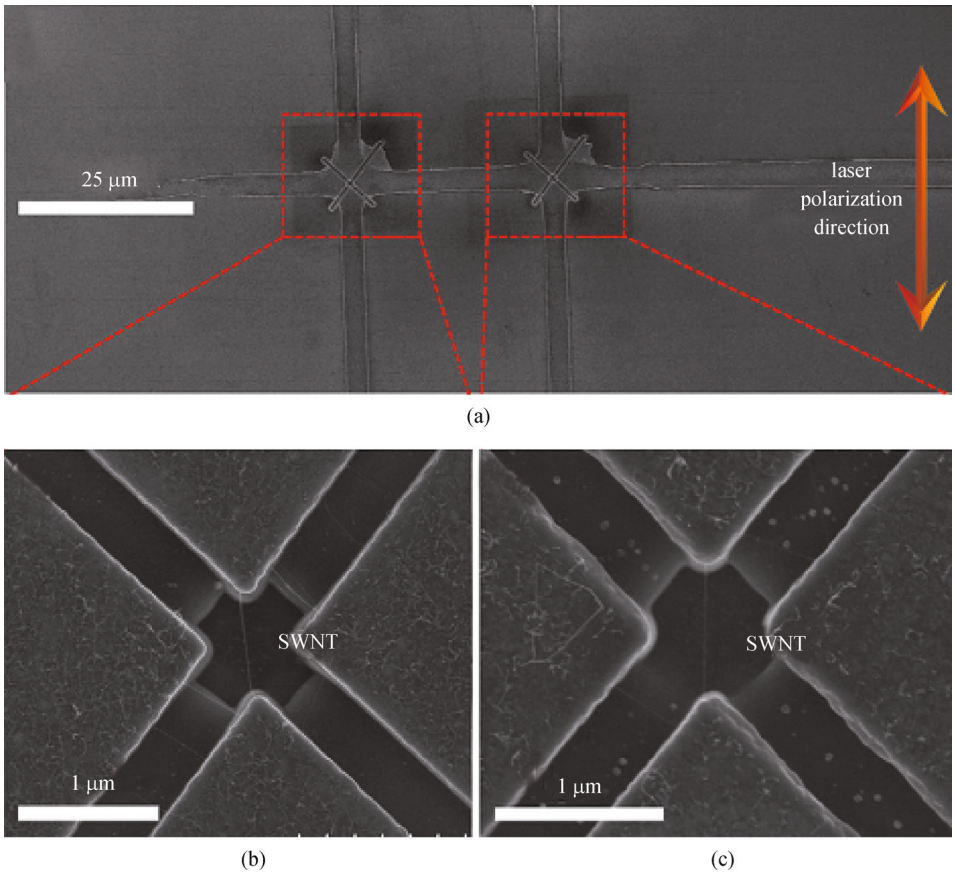

Fig. 11 (a) SEM micrograph of the electrode pattern containing cross-shaped electrodes; (b) and (c) SEM micrographs of the square regions in (a), showing the SWNT-integrated bridge structures [57]

3.2.1 Experimental setup

Figure 14(a) shows a schematic of fabrication process for LDW of graphene patterns. The procedure for graphene fabrication consists of depositing C and Ni thin films sequentially via DC sputtering onto an insulated substrate such as glasses, followed by a femtosecond laser direct writing (FsLDW) process in open air at room temperature. No vacuum chamber is required in this LDW process, which represents an unparalleled way of convenience for graphene fabrication. During the LDW process, a 780 nm fs laser is focused on the Ni film on glass substrate to induce a localized heating for the graphene growth. To avoid the oxidation of the Ni layer during the laser heating process, a layer of immersion oil is applied to cover the Ni surface for preventing the air exposure of Ni during the entire fabrication process. Upon the fs laser irradiation of Ni/C on the glass substrates, due to the ultra-high power density of the laser pulses, highly reactive plasma of Ni and C can be generated and the formation and decomposition of nickel carbide is believed to occur during the short period of laser exposure. Thus, the transformation of amorphous carbon to graphene sheets catalyzed by the Ni film can be achieved under the fs laser irradiation. By moving the sample respective to the focused laser beam via a high resolution piezo stage, arbitrary line patterns of graphene ribbons can be formed directly on the insulated substrates without any graphene transfer process. The whole LDW process can be recorded and well monitored by a charge-coupled device (CCD) camera installed on the optical microscope of the LDW system. After the LDW of graphene patterns, the remaining Ni/C film is removed simply by wet chemical etching process, leaving the as-written graphene patterns on the substrates. Graphene devices can be easily fabricated by additional deposition of metal contacts on the graphene ribbons.

Figure 14(b) shows the graphene pattern of a “G” character under an optical microscope. By simply using computer program, arbitrary 2D graphene patterns can be designed and fabricated using the computer-controlled LDW system. Figure 14(c) shows the 2D band Raman mapping image of the corresponding graphene pattern. The Raman mapping image clearly shows the deposition of graphene patterns on the glass substrate. The uniform color contrast of the Raman image indicates the uniform growth of graphene ribbon by the LDW process.

3.2.2 Characterization of graphene patterns

Various graphene patterns are further demonstrated in Fig.

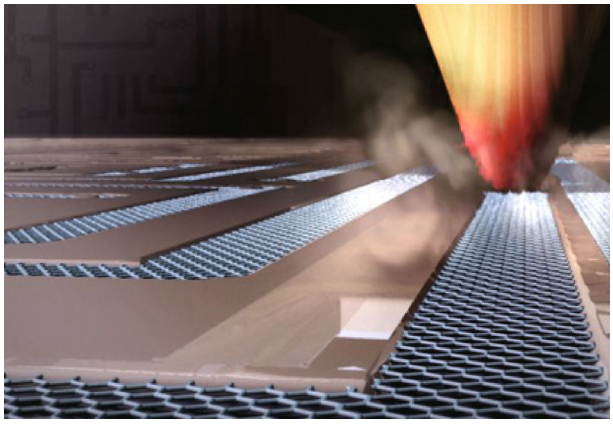

Fig. 12 Illustration of the direct writing process for fabricating graphene nanoelectronics [78]

15, including a "Graphene" text pattern (Fig. 15(a)), a spiral pattern (Fig. 15(b)), arrays of lines (Fig. 15(c)), and an interconnection layout of a NAND logic circuit (Fig. 15 (d)). The feature line-width of the as-fabricated graphene patterns, which is defined by the focal spot size of the fs-LDW system, is confirmed to be around 800 nm as shown in Fig. 15(e). Clear G and 2D bands are observed in a typical Raman spectrum (Fig. 15(f)), which confirms the formation of graphene on the glass substrates. The 2D/G band ratio is close to 1, indicating the formation of bi-layer graphene [84]. A weak D band is also observed in the Raman spectrum due to the existence of graphene edge defects, which is a characteristic of the submicron graphene lines [85]. Transmission electron microscopy (TEM) of the as-fabricated graphene patterns transferred onto Cu grids has also conducted. By charactering the edges of the graphene, the bi-layer structure was clearly observed as shown in Fig. 15(g), which confirms the formation of bi-layer graphene in the LDW method. The optical transmittance of the graphene fabricated via large-area laser scanning on glass substrates were also obtained, as shown in Fig. 15(h). The as-fabricated graphene has a high optical transparency ($>88\%$) in the wavelength range from 300 to 800 nm. The as-measured optical transmittance of the graphene fabricated by the LDW method is 94.3% at 550 nm, which is in consistence to the property of bi-layer graphene [86].

Figure 16 shows the electrical characterization of graphene patterns fabricated on glass substrates. Various graphene patterns with Au contacts were fabricated and tested. Figure 16(a) shows an electrical device structures with four Au electrodes intersected with an array of parallel graphene lines for sheet resistance measurements. The interline spacings of the graphene channels and the Au electrode patterns are 40 and 50 μm, respectively. The *I-V* curve of the electrical devices shows a linear dependence between the channel current and the voltage drop, indicating the metallic characteristics of the graphene lines (Fig. 16(b)). The sheet resistance of the as-fabricated graphene patterns was measured to be (205±19) Ω/sq via the four-probe measurement method, showing a high electrical conductance of the graphene patterns. Comparing with the bi-layer graphene grown via the previous laser-assisted CVD method (~ 400 Ω/sq) [82], this work further reduces the sheet resistance of the graphene patterns by a factor of 2. The high electrical conductance of the as-fabricated graphene patterns is believed to be ascribed to the following two factors: 1) relatively high-quality graphene lattice preserved by the transfer-free

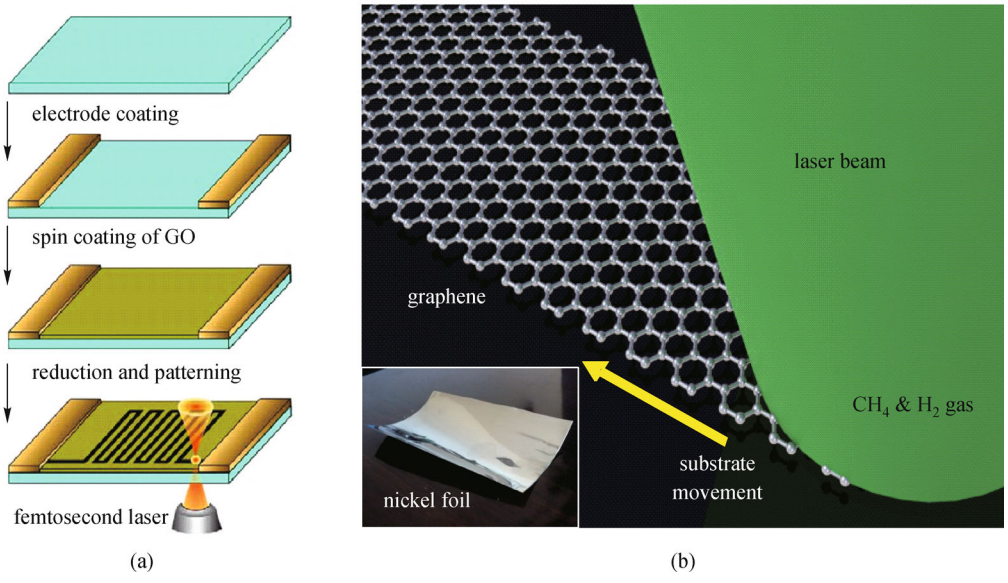

Fig. 13 Two existing fabrication methods of LDW graphene ribbons. (a) Laser-assisted reduction of GO [79]; (b) laser-assisted CVD on Ni foil [81]

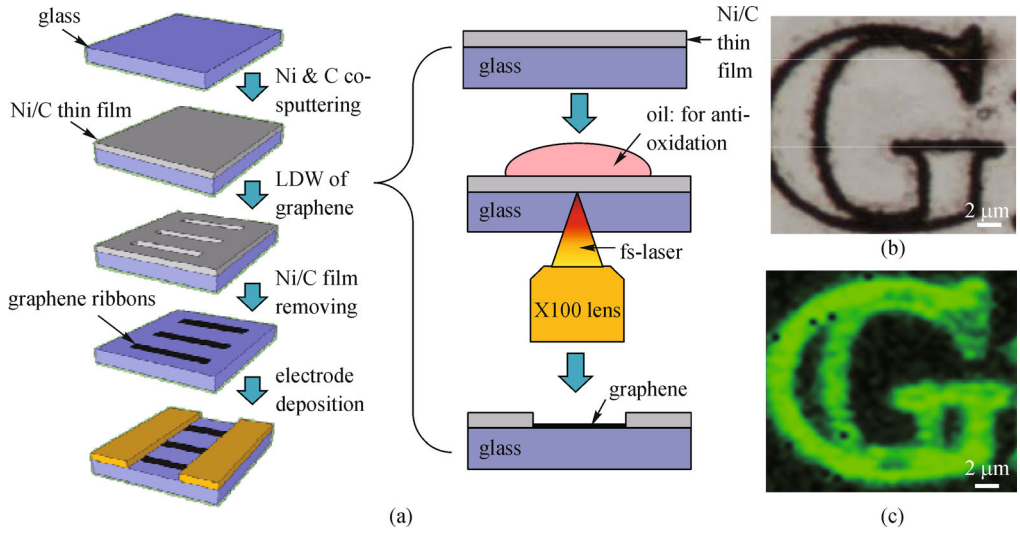

Fig. 14 (a) Experimental schematic of the fabrication process via LDW of graphene patterns in ambient environment; optical (b) and Raman (c) images of the as-fabricated graphene patterns deposited on glass substrates [83]

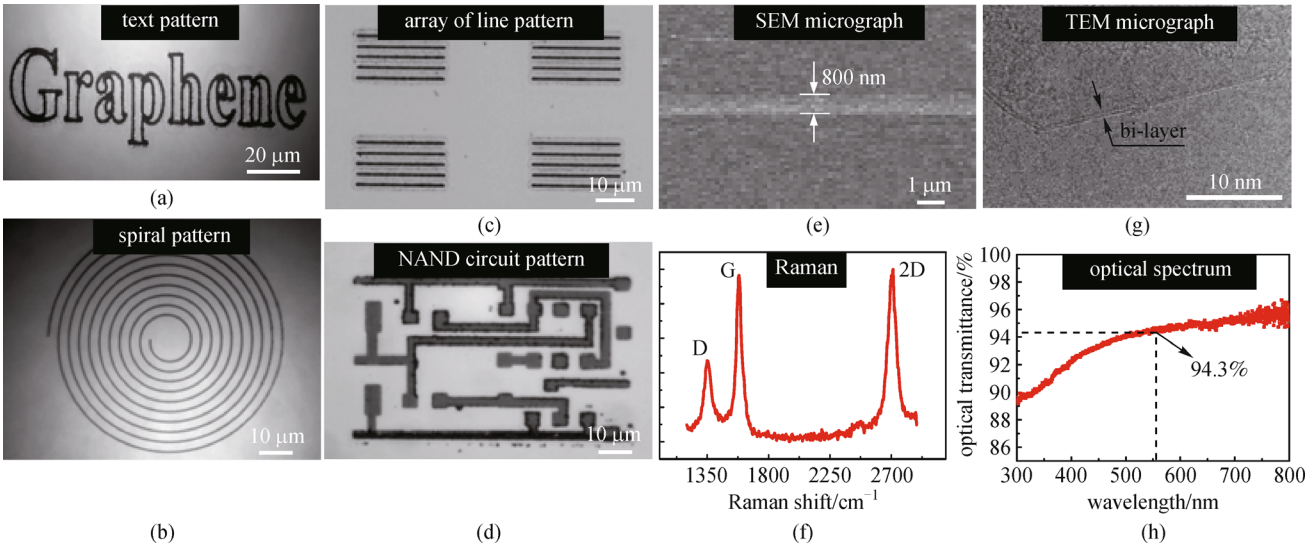

Fig. 15 Characterization of the as-fabricated graphene patterns on glass substrates. Optical micrographs of (a) "Graphene" text pattern; (b) a graphene spiral pattern; (c) arrays of graphene lines; (d) NAND circuit pattern; (e) SEM micrograph of graphene line; (f) typical Raman spectrum of the graphene patterns; (g) TEM micrograph of the graphene transferred on a Cu grid; (h) optical transmittance spectrum of the graphene film on a glass substrate fabricated by the LDW method [83]

growth process; and 2) the existence of Ni doping which are expected to enhance the electrical conductance of the graphene sheets [87,88]. Due to the high electrical conductance, the as-fabricated graphene patterns are promising for various applications such as transparent electrodes, solar cells and smart windows.

To further characterize the carrier density and mobility of the as-fabricated graphene patterns, Hall effect measurements were conducted. As shown in Fig. 16(c), a Greek-cross graphene pattern was adopted in the Hall effect measurements due to two reasons: 1) the low measurement error of the Greek-cross pattern as a van der Pauw test structure [89], and 2) the simple pattern geometry which can be easily fabricated by the LDW method. The majority carrier in the graphene patterns is found to be the hole, indicating the p-type doping of the graphene patterns. The average sheet carrier density and mobility of the as-fabricated graphene at room temperature were measured to be $(11.9\pm2.7)\times10^{12}$ cm^{-2} and (95.7 ± 6) cm^2/(V·s), respectively, which are comparable to the published results [90]. It is noted that the graphene synthesized by the thermal CVD method usually has a high carrier mobility of several thousand cm^2/(V·s) at room temperature [91]. Therefore, the carrier mobility of the as-fabricated graphene by the LDW method at ambient conditions is lower than that of the high-quality graphene

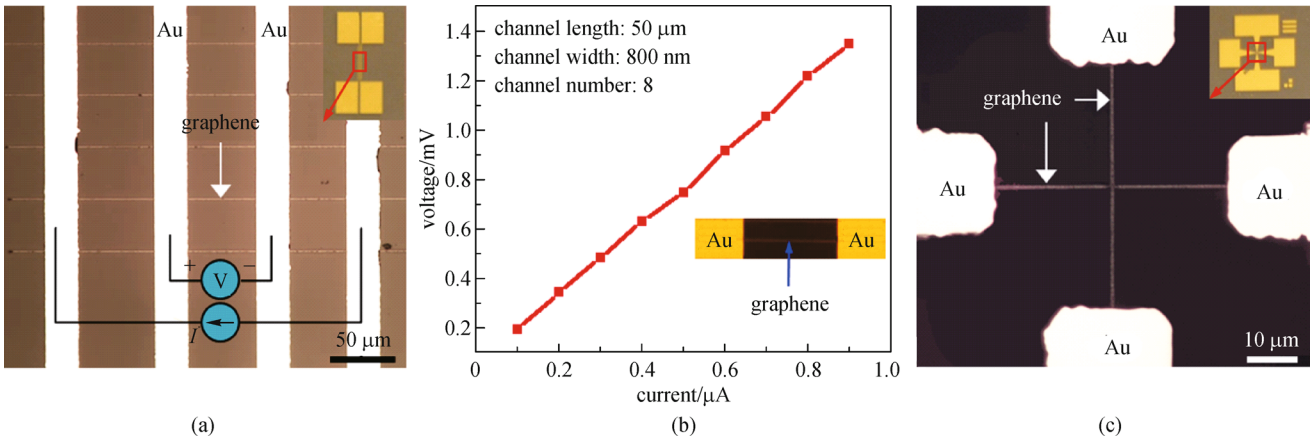

Fig. 16 Electrical characterization of graphene devices fabricated by the LDW method. (a) Optical micrograph of a four-terminal device for sheet resistance measurements; (b) *I-V* curve of the four-terminal electrical device with eight graphene straight line channels as shown in (a), the inset show an optical micrograph of one graphene channel between two Au contacts; (c) optical micrograph of electrical device with Greek-cross graphene pattern for Hall measurements. The insets in (a) and (c) show the zoomed-out optical micrographs of the parallel line and cross-bar graphene devices, respectively [83]

fabricated by the CVD methods, which is believed to be ascribed to the existence of carrier scattering sites by the Ni doping. However, as compared with the reduced GO patterns, the graphene patterns fabricated by the LDW method show a much higher carrier mobility and electrical conductance (for reduced GOs, carrier mobility: 0.1–10 $cm^2/(V \cdot s)$; sheet resistance in kΩ/sq scale) [79,92–94], suggesting a significant improvement of the graphene performance achieved by the LDW method. Moreover, comparing with the conventional CVD based methods which generally requires a temperature of ~ 900°C and Cu substrates for the graphene growth, this LDW method has several apparent advantages: 1) capability to achieve graphene growth at ambient conditions which allows the direct integration of graphene with many external material systems of low heat resistance such as ordinary glasses; 2) direct growth of graphene on target substrates without tedious transfer process; and 3) high flexibility and simplicity for fabricating complex graphene patterns on target substrates, which opens a door for fabricating various advanced graphene-based devices.

3.2.3 Large-scale fabrication of graphene patterns on glass substrates

Based on the optimized conditions for high quality graphene growth, the fabrication of large-scale graphene patterns has been realized. We have developed a semiautomatic fabrication process with software capable of converting a normal geometric data stream (GDSII) file of an integrated circuit (IC) layout (Fig. 17(a)) into a general writing language (GWL) file which is readable by the LDW system (Fig. 17(b)). Therefore, the LDW system can automatically write the graphene patterns on insulating substrates according to the "GWL" file. Large-scale graphene-based IC patterns have been easily fabricated as shown in Fig. 17(c). The successful fabrication of the complex graphene-based IC patterns clearly demonstrates the capability and reliability of the LDW method.

4 Laser direct writing of three-dimensional micro/nano-structures

3D micro/nanofabrication is of increasing interest owing to their importance for the creation of compact 3D devices and their assembly into functional 3D systems. Recent years witnessed a phenomenal increase for the 3D micro/nanofabrication techniques from diversified fields, such as MEMS/NEMS, nanoelectronics, micro/nanophotonics, biomedical engineering, bio-inspired architectures, and micro/nanofluidics, with the aim of developing neo-conceptual and high-value-added products [95–101]. Currently, most 3D micro/nanofabrication techniques are based on traditional 2D fabrication techniques, such as photolithography, using lay-by-layer strategies. However, such 3D micro/nanofabrication techniques provide only limited 3D micro/nanofabrication capabilities. Broad applications of such 3D micro/nanofabrication are limited due to expensive facilities, time-consuming layer-by-layer strategy, high cost, low throughput, and the incapability in fabricating 3D micro/nanostructures of arbitrary geometry and increased complexity. Some applications would be extremely challenging by using conventional micro/nanofabrication techniques, such as the controlled introduction of defects into 3D photonic crystals to achieve required functionality, fabricating 3D movable components in MEMS/NEMS devices, and constructing micro/nanofluidic devices. Therefore, a 3D micro/nanofabrication technique that capable of fabricating 3D micro/nanostructures of arbitrary geometry at a nanometric resolution in a cost-effective process is highly desired.

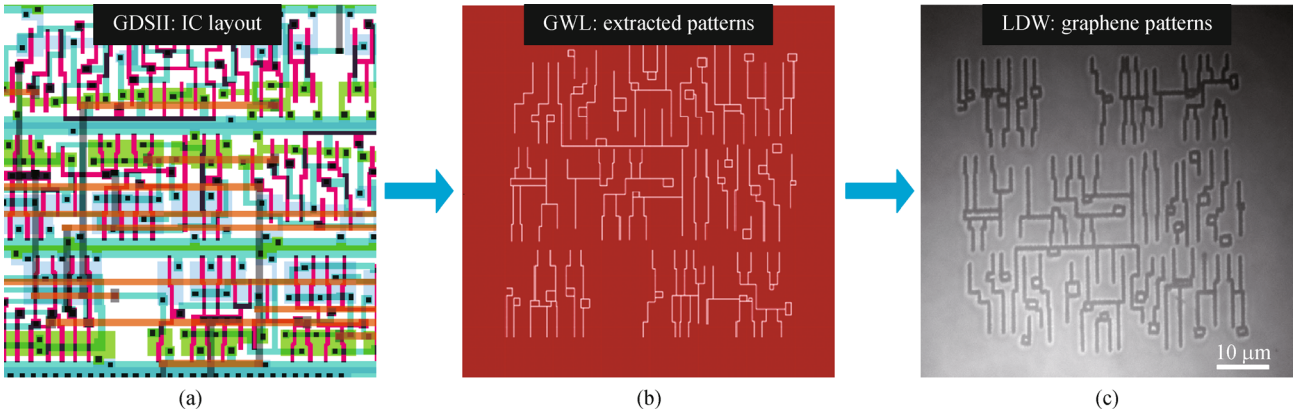

Fig. 17 Flow chart of large-scale fabrication of graphene patterns toward the manufacture of graphene-based integrated circuits. (a) IC layout in the GDSII format; (b) an extracted metal layer layout in the GWL format; (c) fabricated graphene patterns on a glass substrate [83]

Femtosecond laser direct writing (FsLDW) is a laser-based precise 3D micro/nanofabrication method, and has been recently recognized as a promising candidate to address the existing challenges [20,102–106]. In FsLDW, a tightly focused laser beam penetrates into a bulky material without obvious absorptive energy loss, and scans according to a designed pattern from the bottom slice to the upside slice or vice versa until the entire 3D structure is fabricated [20]. Due to the extremely high transient power density, photons are absorbed in a nonlinear manner at the focal point in a volume much smaller than the cubic wavelength, λ^3, achieving high spatial resolution, beyond the optical diffraction limit [20]. Therefore, FsLDW can be simply understood as a LDW technique, which involves nothing more than converting a 3D digital design into a target material. FsLDW also distinguishes itself from other micro/nanofabrication methods as a universal tool applicable to diversified materials, including organic materials, biomaterials, dielectrics, metals and semiconductors, only if a proper photon-material strategy is determined [20]. Compared with conventional 3D nanofabrication techniques, FsLDW demonstrates several advantages, including 1) single-step noncontact and mask-free direct 3D fabrication, 2) capable of fabricating arbitrary geometries and irregular structures, 3) capable of fabricating movable components, 4) realization of real 3D nanofabrication, 5) working on a broad range of materials such as polymers, ceramics, metals and hybrid materials, and 6) easy fabrication of voids, channels and holes inside a bulk material [102].

In this section, the 3D micro/nanofabrication based on FsLDW will be introduced. Two different 3D micro/nanofabrication strategies will be demonstrated, including the additive 3D micro/nanofabrication by two-photon polymerization (TPP) and the subtractive 3D micro/nanofabrication by multi-photon ablation (MPA). The advantages and disadvantages for both fabrication techniques will be shown and analyzed. Finally, a comprehensive 3D micro/nanofabrication method by seamless integration of the additive TPP and subtractive MPA will be demonstrated. The established comprehensive 3D fabrication method not only inherits the merits of both TPP and MPA in achieving ultrahigh writing resolution beyond the diffraction limit and features of sharp and clean edges, but it also offers the possibility to produce novel device structures which are difficult to be fabricated by either TPP or MPA alone.

4.1 Additive 3D micro/nanofabrication using two-photon polymerization

TPP is one of the additive FsLDW techniques making use of photosensitive resins in 3D micro/nanofabrication. Compared with other micro/nanofabrication approaches, additive TPP lithography offers both high resolution and relatively high throughput. TPP lithography is a typical nonlinear optical effect which, in general, requires a femtosecond (fs) laser to provide short pulses with photon energy well below the one-photon absorption edge of a photoresist. Polymerization of the photoresist takes place if the light intensity is high enough for two-photon absorption inside the material, which is in the focal volume of a microscope objective. This process causes a chemical and/or physical change of the photoresist within a small volume pixel (“voxel”). This voxel typically is of ellipsoidal shape and is the basic building block in the 3D fabrication process. By moving the sample relative to the fixed focal position, arbitrary paths can be written into the photoresist. It can be simply described as using a laser beam to inscribe nanostructures in three dimensions. Because of the threshold behavior and nonlinear nature of the process, a resolution far beyond the diffraction limit can be realized by controlling the laser power and scanning speed. As a result, the technique provides much better structural resolution and quality than conventional stereolithography methods.

The 3D micro/nanofabrication system installed in our laboratory (Nanoscribe GmbH) mainly consists of a fs laser, a piezoelectric 3D scanning stage for fast writing of small-area structures, and a motor-driven linear positioning system. The laser is a compact fs-fiber laser (Menlo Systems, T-Light II) with 65 mW average power, 780 nm center wavelength, a pulse duration below 120 fs and a repetition rate of 100 MHz. The piezo positioning system, with *X*-*Y*-*Z* axes, provides a maximum travel distance of 300 μm in each direction. The Zeiss optical microscope equipped with a CCD camera enables real-time process monitoring. The whole system is installed on a vibrational isolation table from Thorlabs Inc.

It generally takes three steps in TPP micro/nanofabrication. First, a glass substrate is coated with a layer of photoresist and loaded into the lithography system. The second step is structure programming by using a specialized general writing language (GWL). Alternatively, the structure data can be also imported from a CAD or a stereolithography file (STL). The 3D lithography system visualizes the loaded structure data and automatically approaches the designated samples and adjusts the focus to the interface. Finally, the 3D lithography system conducts the TPP process by tightly focusing the laser beam inside the photoresist and making 3D scan according to the geometry design. After the TPP lithography, the samples are developed and post-processed for further experiments.

The basic building block of TPP is so called "voxel" of polymer. Systematical study of the feature size of the voxel with respective to the laser scanning speed and power is critical and it can promote the understanding on the TPP process and provide guidance to control the fabrication geometry in the additive TPP process. To study the voxel size, series of suspended polymeric lines was first fabricated with different laser scanning speed, laser average power and writing depth, since the transverse size of a polymeric line fabricated by one laser scan reflects the corresponding voxel dimension. Then, after the developing process, the fabricated polymeric lines will be characterized under a SEM. Due to the high spatial resolution of SEM, the voxel size in both lateral and vertical dimensions under different TPP conditions (different laser power and scanning speed) can be precisely obtained. Therefore, a database of voxel dimension with respect to different TPP conditions including laser scanning speed, average power was established. Such a database is critical and important not only for the precise additive 3D micro/nanofabrication but also for the mechanism study of the ultrafast laser-material interactions. Figure 18 shows the characterization of voxel size in the TPP process using IP-L photoresist (Nanoscribe GmbH). The lateral and vertical dimensions of the voxel increase as the laser scanning speed increases. However, the lateral and vertical dimensions of the voxel start to decrease when the laser scanning speed reaches a certain point. The positive correlation between the voxel dimensions and the laser scanning speed within 0–50 μm/s range contradicts to the conventional TPP process, in which the voxel size should grow correspondingly by increasing exposure time or reducing laser scanning speed. It is suggested that the IP-L photoresist applied in our TPP process may have a laser-induced deactivation effect during the additive micro/nanofabrication process which is similar to the stimulated emission depletion (STED) effect as applied in fluorescence microscopy by Hell and Wichmann [107].

Besides the calibration of voxel dimensions with different laser powers and scanning speeds, the optimization of laser scanning modes was also conducted. Practical applications of micro optical devices, such as micro-lens, generally require high quality surface profile and sufficient smoothness. Therefore, it is important to optimize the TPP process for the fabrication of 3D micro/nanostructures with sufficient surface smoothness. In the TPP process, we found that conventional parallel linear scanning mode can

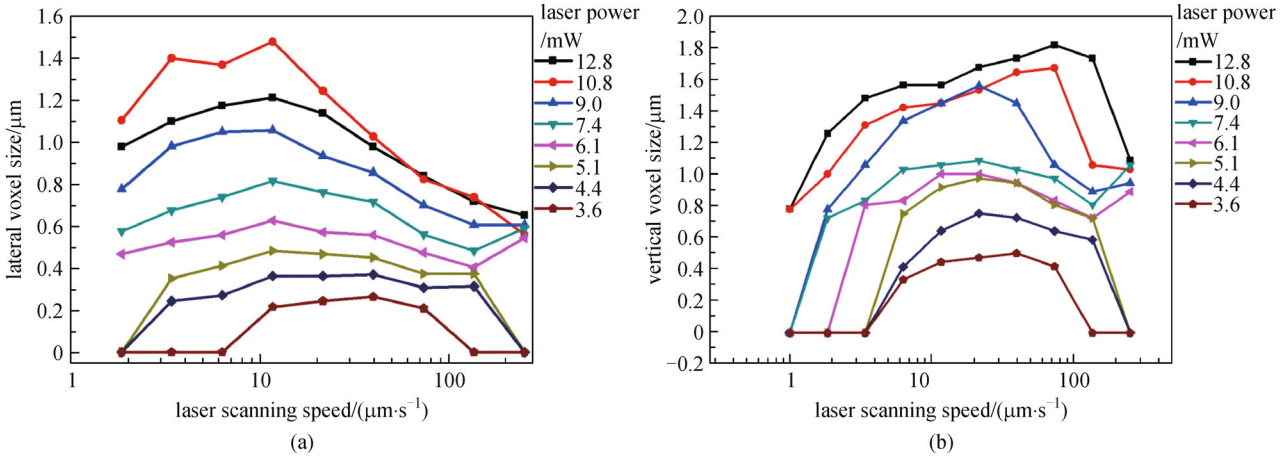

Fig. 18 Characterization of voxel sizes in the additive TPP process. (a) Lateral and (b) vertical voxel sizes as a function of laser scanning speed at fixed laser power

hardly get high quality surface. In fact, during the parallel linear scanning, it can be imagined that the width of the fabricated line will make not only the deformation of circle dimension but also protrusions at the edges of the lens surface, as shown in Figs. 19(a)–19(c). To obtain smooth micro-lens with better optical performance by TPP lithography, an annular scanning mode cooperated with continuous variable scanning steps was adopt. By using this new scanning method, spherical micro-lens with high surface quality was readily produced with a shorter processing time, as shown in Fig. 19(d).

Figure 20 show that a variety of 3D photonic crystal structures have been fabricated using the additive TPP technique with a spatial resolution around 150 nm. Compared with 2D photonic crystals, 3D photonic crystals provide the capability to manipulate light regardless of the polarization direction due to their omnidirectional photonic band structures coming from corresponding solid network structures [108]. Therefore, 3D photonic crystals can avoid many disadvantages of 2D photonic crystals. However, such 3D photonic crystals are very challenging and costly to fabricate using conventional approaches. It is demonstrated that TPP provides a powerful tool in the convenient fabrication of functional 3D photonic crystals. Other than the 3D photonic crystal structures, many other 3D optical components and structures were successfully fabricated by the additive TPP micro/nanofabrication process. Figures 21 and 22 demonstrate SEM micrographs of the micro-lens arrays, optical cavity structures and various complex 3D micro-logos. The fabrication results demonstrate the

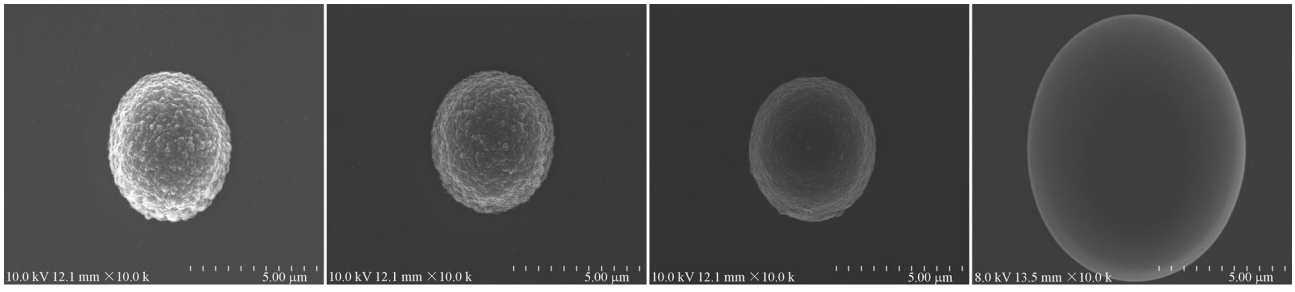

Fig. 19 Dependence of surface quality of 3D structures on different laser scanning parameters: parallel linear scanning mode of (a) 200-nm step; (b) 100-nm step; (c) 20-nm step, 1 h processing time; (d) annular scanning mode, 10-nm step, 20 min processing time

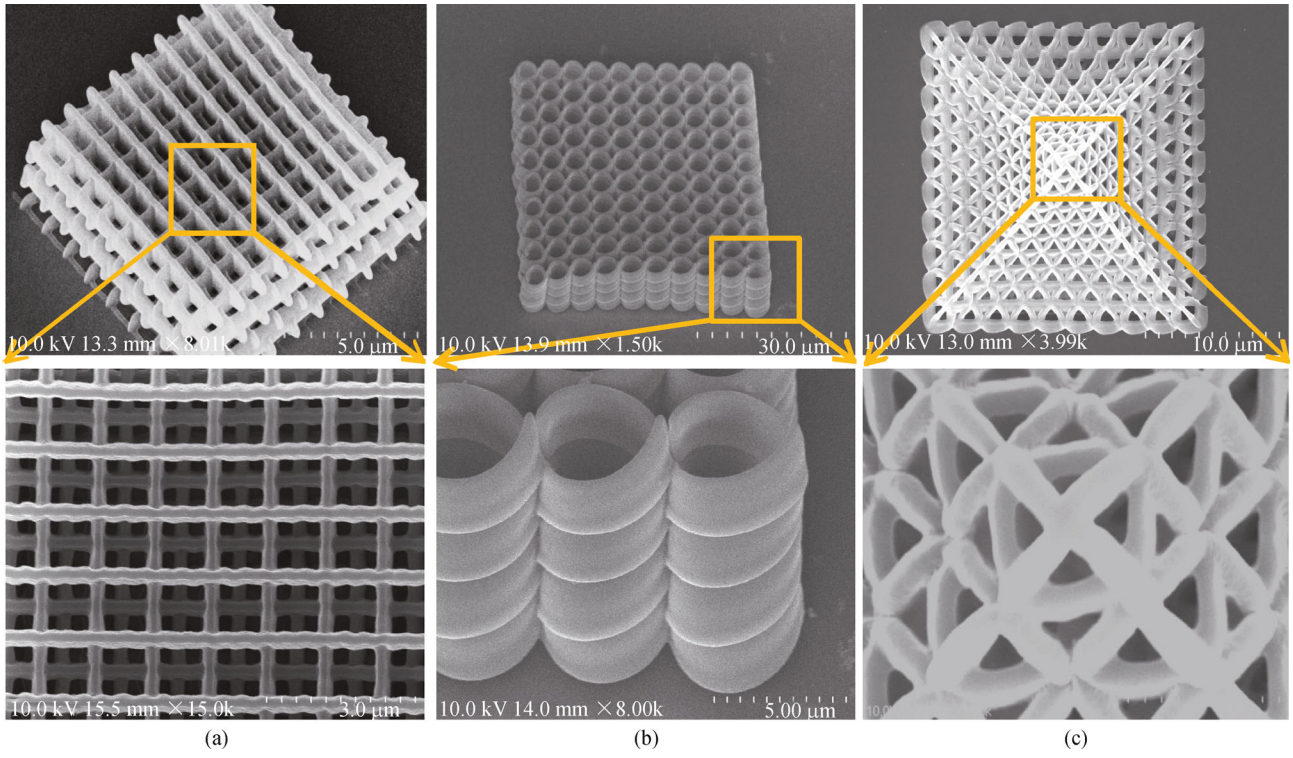

Fig. 20 SEM images of various photonic crystal structures fabricated by additive TPP micro/nanofabrication. (a) Woodpile structures; (b) spiral arrange structures; (c) pyramid structures

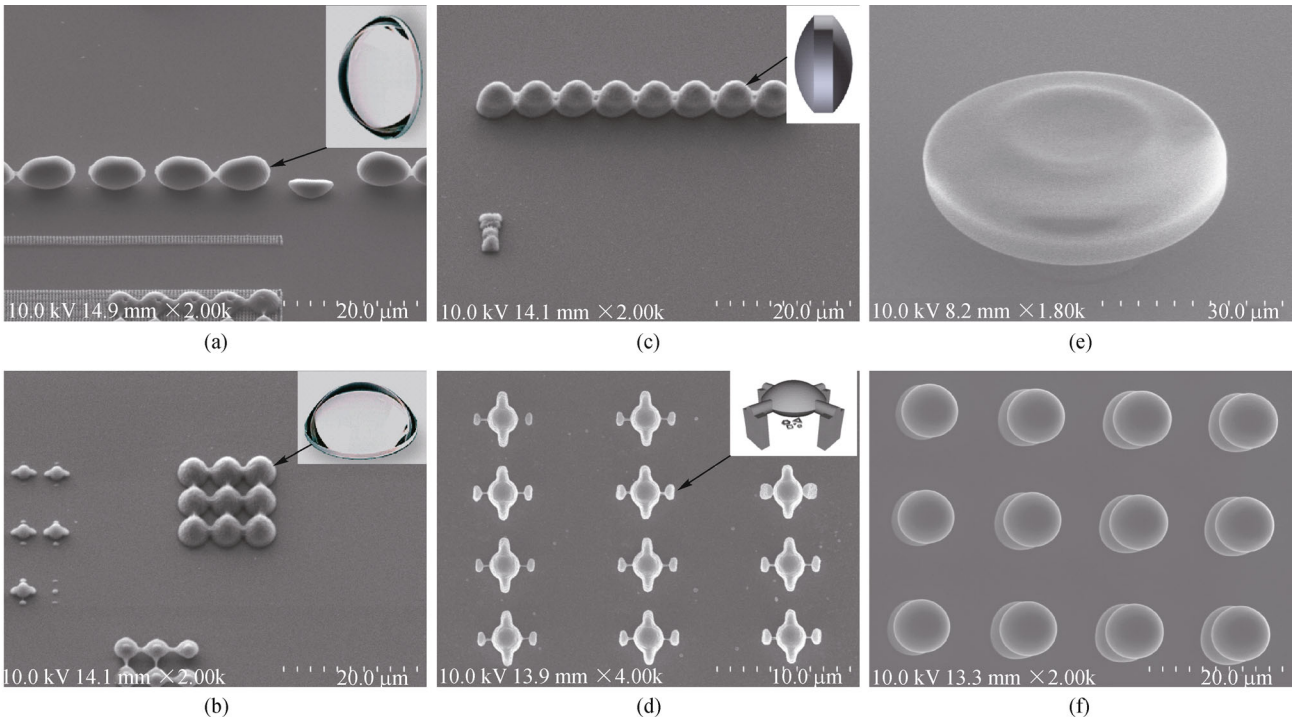

Fig. 21 SEM images of micro-lens arrays and optical cavity structures fabricated by additive TPP micro/nanofabrication. (a) Vertically-aligned aspheric lens array; (b) horizontally-aligned aspheric lens array; (c) vertically-aligned bi-convex lens array; (d) horizontally-aligned bi-convex lens array; (e) disk-shaped optical cavity for dye laser application; (f) spherical micro-lens array

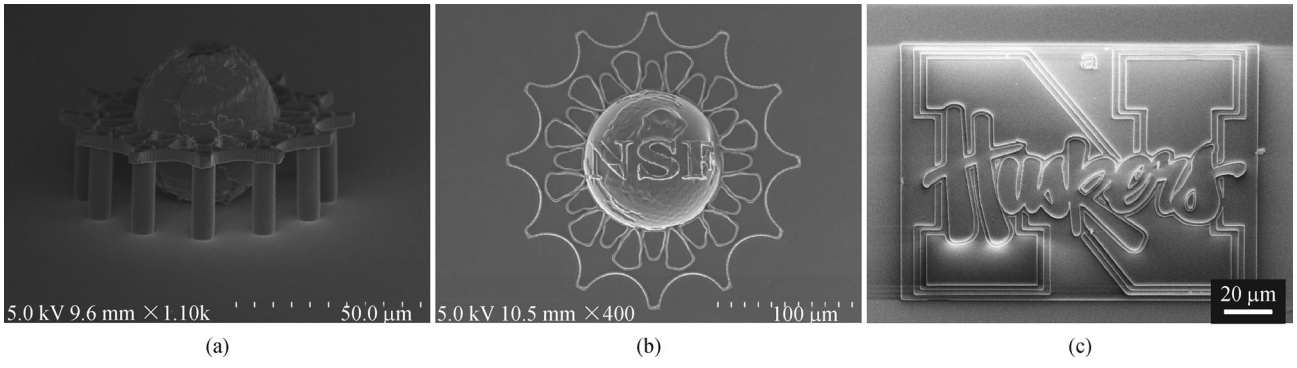

Fig. 22 SEM images of some examples of complex 3D structures fabricated by additive TPP micro/nanofabrication. (a) Side-view of a 3D NSF logo; (b) top-view of 3D NSF logo; (c) 3D Nebraska-Huskers logo

capability of the TPP method in precisely fabricating 3D micro/nanostructures of complicated geometries.

4.2 Subtractive 3D micro/nanofabrication using multi-photon ablation

MPA is another typical FsLDW technique, which has been established as a useful subtractive manufacturing technology in 3D micro/nanostructuring solid materials by direct ablative writing [109–111]. MPA requires simultaneous absorption of multiple photons in a single quantum event to initiate the ablation [112]. Multiphoton absorption produces initial free electrons that are further accelerated by the fs laser electric field [112]. These electrons induce avalanche ionization and optical breakdown, and generate localized plasma [112]. The subsequent expansion of the localized plasma results in the fabrication of a void structure at the focal point [112]. Due to the nature of nonlinear interaction, a high resolution beyond diffraction limit can be obtained. A variety of micro/nanostructures have been fabricated by the MPA process. Chichkov et al. reported the fabrication of a photonic crystal structure with a defect cavity at the center by creating periodic nanostructures in sapphire using MPA [112]. Sun et al. reported the fabrication of 3D photonic crystals within silica [113]. Zhou et al. fabricated the first void-dot face

centered cubic (fcc) 3D photonic crystal in lithium niobate with a pronounced high-order stop gap at wavelength 1.5–2 μm [114]. It is noteworthy that, due to the femtosecond pulse duration electron-photon interaction ranging in the picosecond regime are minimized, thus thermal effects are almost negligible with minimum edge-effects [110]. Therefore, MPA is especially capable in fabricating structures like channels, holes and voids in various materials [109–111,115–117].

We have used the same laser lithography system for carrying out the subtractive MPA fabrication. The experimental setup is similar to the TPP fabrication process except that significant higher laser powers than the TPP process (2–7 times higher) are required. Cured IP-L polymers were used as the raw material which promises a high spatial resolution beyond diffraction limit. Due to the short pulse duration of the fs laser (120 fs) which is much shorter than the electron-phonon coupling time (~1 ps) [118], there is limited heat exchange between the irradiated area and the surroundings during the subtractive MPA process, resulting in stable and reproducible subtractive fabrication with minimized thermal stress and collateral damages. Figure 23(a) shows an array of holes created by MPA in an IP-L film of 200 nm thick. A magnified image of one hole is shown in the inset of Fig. 23(a). The diameter of the holes is around 180 nm, far beyond the diffraction limit of the laser beam. In addition, Fig. 23(b) shows five interconnected hollow rings resembling Olympic Rings created inside a cured IP-L polymer film. The channel width is 1 μm with a sharp and clean ablation edges.

4.3 Comprehensive micro/nanofabrication

Although both additive and subtractive micro/nanofabrication methods are established separately, they have been largely isolated. Fabricating advanced devices of complex 3D geometries calls for the use of both additive and subtractive processes. For example, a seamless spherical shell is difficult to be fabricated by either additive or subtractive process. In additive processes, the solid shell of the sphere prevents the dissolving of unexposed photoresist inside the sphere to produce a void. While in subtractive processes, a solid sphere has to be created before subtracting the inner part to make a hollow shell. Therefore, a comprehensive 3D micro/nanofabrication method possessing both additive and subtractive functionalities is not only desirable but also in demand for advanced device fabrication.

We successfully integrated an additive TPP and a subtractive MPA process into a single FsLDW system in which process conditions could be precisely controlled. The integrated fabrication method not only inherits the merits of both TPP and MPA such as writing resolution smaller than the diffraction limit and features with sharp and clean edges, but it also offers the possibility to produce novel device structures which are difficult to be fabricated by either TPP or MPA alone.

Figure 24 shows a schematic design of the integrated 3D micro/nano fabrication system combining both additive TPP and subtractive MPA processes. The whole fabrication process consists of three steps. First, TPP is employed to fabricate 3D solid microstructures inside the negative photoresist of IP-L (Nanoscribe GmbH). Second, unsolidified IP-L photoresist is washed away by rinsing the sample in isopropyl alcohol (99.5%, BDH) for 20 min. Third, a subtractive process based on MPA is carried out in air to tailor the cured IP-L to a desired 3D geometry. Depending on the size of the desired structure, TPP is performed by using laser average powers that vary between 3.5 and 8 mW. MPA instead, requires a laser average powers which are 2–7 times higher than that used

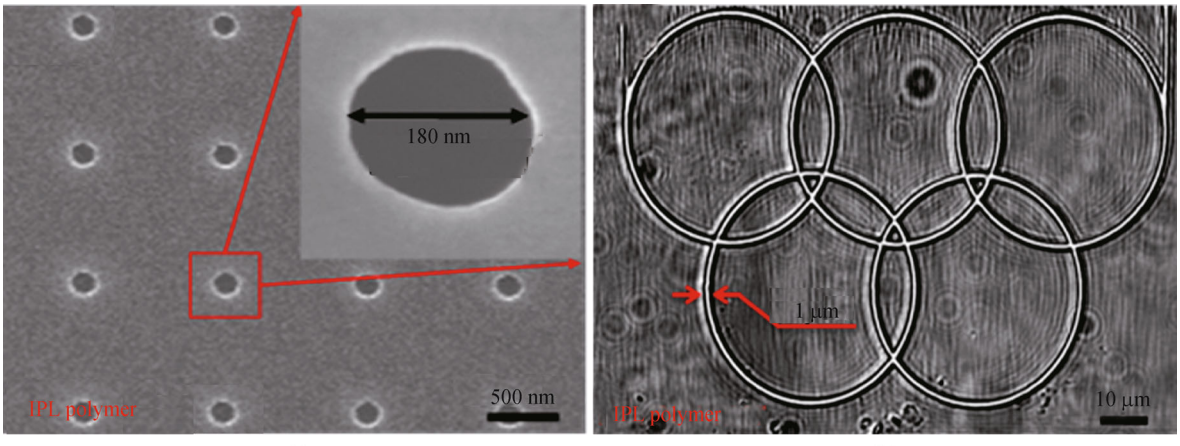

(a) (b)

Fig. 23 Micro/nanostructures fabricated by the subtractive MPA process in cured IP-L polymer films. (a) SEM micrograph of nano holes, the inset is a magnified image of a hole with a sharp edge and a pore diameter of 180 nm; (b) optical image of five micro-sized interconnected hollow rings resembling Olympic rings embedded in a cured IP-L polymer film created by MPA [119]

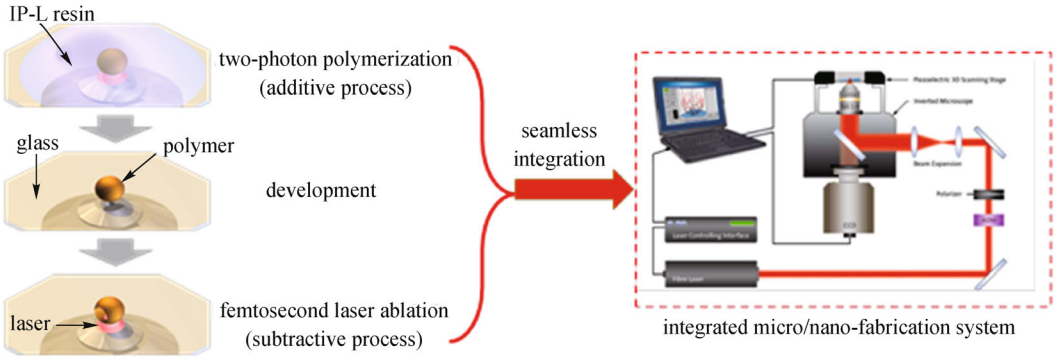

Fig. 24 Schematic diagram of the comprehensive 3D micro/nanofabrication combining additive TPP and subtractive MPA processes [119]

for TPP. The laser beam is generated by a mode-locked fs fiber laser (780 nm central wavelength, 100 MHz repetition rate, and 120 fs pulse duration) and it is tightly focused within the sample by an oil-immersion objective lens (1.4 NA, 100 ×). Writing in both additive and subtractive processes is achieved by moving the sample around a fixed laser beam by means of a computer-controlled *X-Y-Z* piezo stage.

To demonstrate the capabilities of the "TPP + MPA" method in 3D micro/nano fabrication, we fabricated two kinds of device structures. The first one is shown in Fig. 25 and it consists of arrays of microstructured polymer fibers with different diameters. TPP process was employed to fabricate these structures with 2, 1, and 0.5 μm linewidths, as shown in Figs. 25(a), 25(c), 25(e), respectively. The laser average power and stage scanning speed employed for TPP were 7 mW and 100 μm/s, respectively. And the different linewidths of the fibers were achieved by controlling the number of laser passes in fabricating a single polymer fiber. Upon polymerization, the refractive index of IP-L increases to a value of 1.52. Therefore, the polymer fibers could be used as light waveguides for integrated optics [120]. Following TPP, a subtractive MPA process was performed with laser average power of 26 mW, laser exposure time of 5 ms per spot, and stage scanning speed of 100 μm/s. Periodic hole patterns with ~500 nm in diameter were fabricated along the polymer fibers to form Bragg grating structures in waveguides, as shown in Figs. 25(b), 25(d), 25(f). The diameter and the periodicity of the holes were tunable by adjusting the laser average power, exposure time and scanning speed. It is noteworthy that the fiber Bragg gratings as shown in Fig. 25 are difficult to be fabricated by either TPP or MPA alone.

The second type of device structures fabricated by implementing TPP and MPA is shown in Figs. 26 and 27, where meshed and spiral micro-fluidic channel systems are represented, respectively. First, polymer cubic structures were fabricated by the additive process of TPP on glass substrates. Then, interconnected micro-channels were directly written within the polymer microstructures via the subtractive process of MPA. The laser average power and the scanning speed employed to create the channels were 26 mW and 50 μm/s, respectively. Figures 26(a) and 26(b) clearly show the typical micro-channels created by MPA. The diameter of the channel is about 1 μm according to the SEM characterization. Figure 26(c) shows the meshed micro-fluidic channel system created inside the IP-L polymer cube. Liquid flows through the meshed channels can be clearly observed in Figs. 26(d) and 26(e), which verifies the hollow structure and the connectivity of the micro-fluidic channels. Besides the 2D meshed channels, 3D spiral micro-channels were also successfully fabricated inside the IP-L polymer. Figure 27(a) shows a schematic structure of 3D spiral channel inside a polymer cube. The labels of "A" and "B" in Fig. 27 refer to two points which are the highest and the lowest in *Z* direction respectively. The optical microscope image of the spiral channel changes as the focal plane of observation shifts from low to high as shown in Figs. 27(b) – 27(d), which indicates the 3D characteristics of the spiral micro-fluidic channel created inside the IP-L polymer. By using the "TPP + MPA" method, arrays of the spiral micro-fluidic channels with a user-defined spacing can be readily fabricated as shown in Fig. 27(e). Comparing with the mainstream technique of soft-lithography for fabricating micro-fluidic systems [121], the "TPP + MPA" method holds several advantages. First, it is a mask-free process. It provides an unparalleled convenience and freedom in prototype design with a computer-aided design program without the need to fabricate replica molds as always required by the soft-lithography method. Second, it is a truly 3D fabrication method in contrast to the soft-lithography which is inherently limited to 2D processing due to the requirement of molding. And third, it needs no sealing of micro-channels which is a necessary fabrication step in the soft-lithography process.

5 Conclusions

All of the grand goals for nanoscience are dependent upon

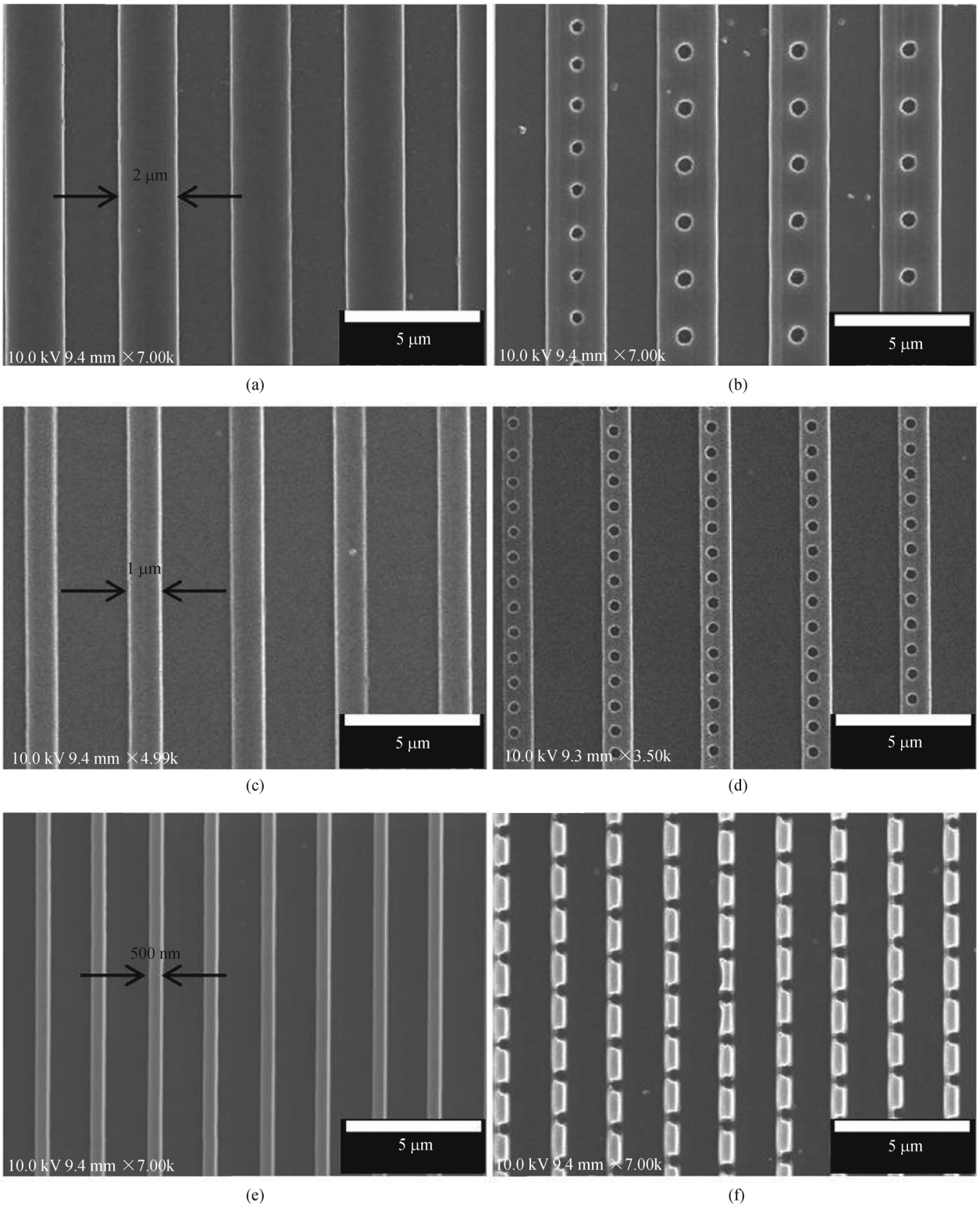

Fig. 25 SEM images of polymer fibers fabricated by the "TPP + MPA" method. (a), (c), (e) The arrays of fibers created by TPP with 2, 1 and 0.5 mm in diameters, respectively; (b), (d), (f) the arrays of fibers with periodic hole patterns after the MPA process [26]

reliable ways to fabricate nanostructures. In this review, we have summarized the recent development in applying laser based material processing approaches in fabrication of various nanomaterials and micro/nanostructures of various dimensions which are challenging to be fabricated via conventional fabrication methods. Research efforts are

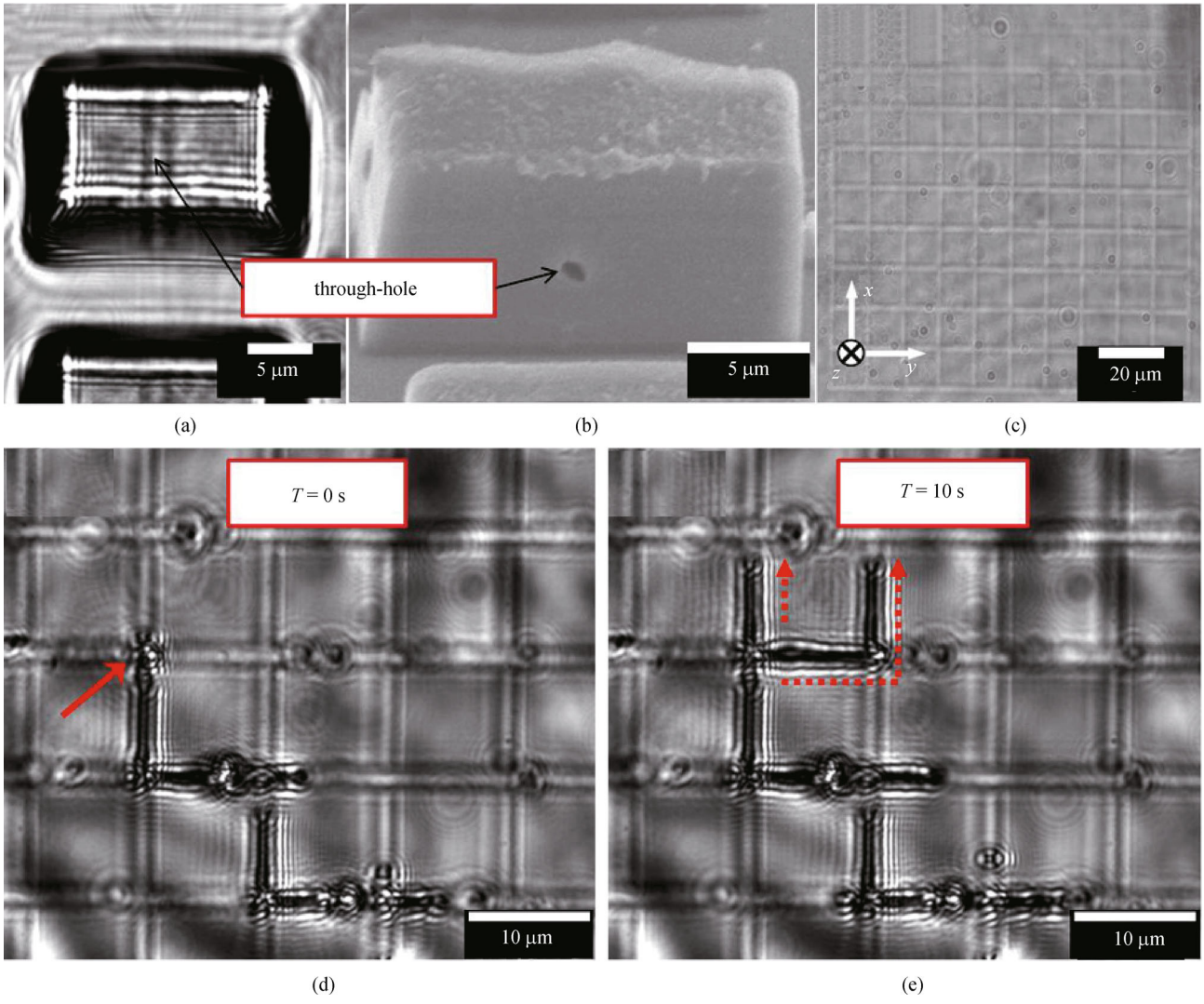

Fig. 26 2D meshed micro-fluidic channels inside IPL polymer fabricated by the "TPP + MPA" method. (a) Optical micrograph of a typical micro-fluidic channel inside a polymer cube; (b) SEM cross-section image of the micro-fluidic channel; (c) optical micrograph of the fabricated meshed micro-fluidic channels; (d) and (e) demonstrate the liquid flow inside the meshed channels at $T = 0$ and $T = 10$ s, respectively. The dash line shows the pathway of liquid flow through the meshed micro-fluidic channels [26]

focused on developing laser based processing techniques for fabricating 1D, 2D and 3D nanomaterials and micro/nanostructures.

For the growth and assembly of 1D nanomaterial of carbon nanotube, a novel laser-assisted CVD (LCVD) process was developed. The LCVD process was demonstrated as an efficient method for growing the carbon nanotubes. Comparing with the conventional CVD process, LCVD has provided several unique advantages such as much shorter heating and cooling cycle for the entire process and capability of localized processing. Furthermore, its inherent and unique secondary effects of laser interaction with matters such as optical near-field enhancements offer it further controllability on synthesis location and orientation of single-walled carbon nanotubes (SWNTs) during LCVD process. Well controlled SWNT-bridge structures with individual suspended SWNT channels were successfully fabricated using the LCVD process. The significant optical near-field enhancement at the electrode tips and its dependence on the laser polarization and metallic film thickness were studied and verified by numerical simulation and experimental results. The SWNT growth is tightly confined around the electrode tips at low substrate temperature. Comparing with previous SWNT assembly/integration methods, the optically controlled assembly method during LCVD possesses a number of advantages including: precise SWNT placement control, in situ one-step growth process, low substrate temperature and reliable SWNT/metal contacts. These advantages make the LCVD method a potentially promis-

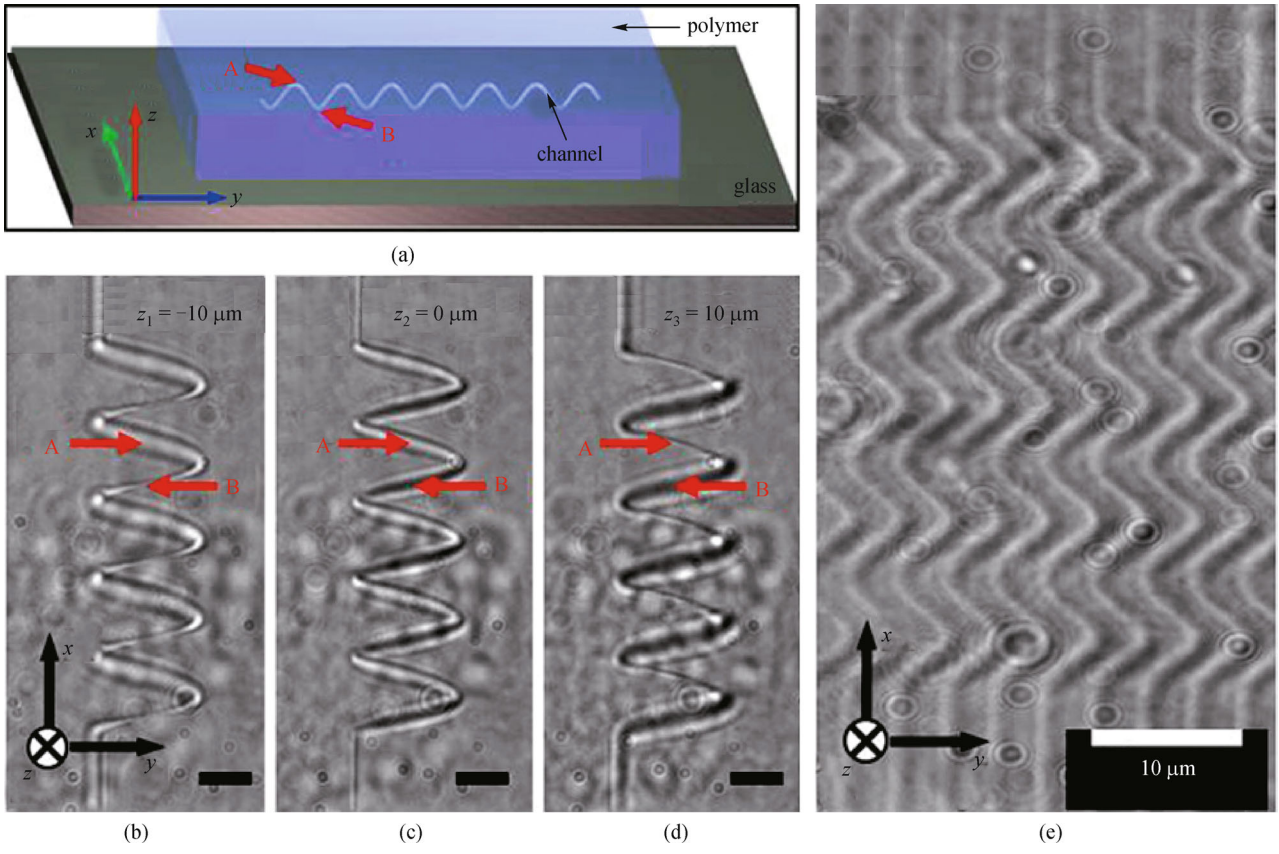

Fig. 27 3D spiral micro-fluidic channels inside a IPL polymer cube fabricated by the "TPP + MPA" method. (a) Schematic of the 3D spiral micro-fluidic channel; (b), (c), and (d) show the *X-Y* cross-sectional view of a spiral channel under a transmission-mode optical microscope at different focal planes (scale bar: 10 μm). The coil diameter of the spiral channel is 20 μm; (e) array of spiral micro-fluidic channels fabricated inside a polymer cube with a coil diameter of 5 μm and an inter-channel spacing of 3 μm [26]

ing technique for future mass production of SWNT-based nanoscale devices.

For the fabrication of 2D nanomaterial of graphene patterns, a laser direct writing (LDW) process at ambient conditions was proposed and developed. Femtosecond laser combined with a high resolution *X-Y* piezo stage was used to write complex graphene patterns on nickel/carbon/glass. After the laser writing process, the remaining Ni top-layer can be simply removed through chemical etching process leaving only the as-written graphene patterns on the glass substrates. The proposed fabrication method can get rid of the expensive and relatively slow thermal CVD process in a vacuum chamber and achieves the open-air and room-temperature growth of the graphene patterns directly on the insulated substrates without any transfer process. Large-scale graphene patterns of practical integrated circuits were successfully fabricated and demonstrated. Considering its simplicity, designability and highly-reliability in producing graphene patterns, this LDW method could pushes current graphene research closer to the real practical applications.

For the fabrication of 3D micro/nanostructures, research efforts have been focused to establish a truly 3D micro/nanofabrication platform based on the femtosecond LDW (FsLDW) techniques. Both additive two-photon polymerization (TPP) and subtractive multi-photon ablation (MPA) techniques for 3D micro/nanofabrication have been developed separately based on this platform. The successful fabrication of a wide range of 3D micro/nanostructures by either TPP or MPA processes has proven the usefulness and efficiency of TPP and MPA in 3D micro/nanofabrication. Furthermore, a comprehensive and versatile 3D micro/nanofabrication method has been developed by integrating both additive TPP and subtractive MPA processes into a single FsLDW framework. The nonlinear characteristics of the fabrication processes offer a writing resolution below 200 nm, far beyond the optical diffraction limit. In addition, this method also inherits the virtues of MPA in creating sharp and clean processing edges due to the minimized thermal stress and collateral damages. Results show that the combination of additive and subtractive fabrication processes enables the fabrication of complex 3D micro/nanostructures which are difficult for either TPP or MPA alone. It is believed that this new 3D

micro/nanofabrication method paves the way for the development of advanced devices such as integrated optical circuits and laboratory-on-a-chip devices.

Acknowledgements This research work was financially supported by the National Science Foundation (Nos. CMMI 1265122, 0555884, 0900419, 0758199 and ECCS 0621899, 0621899, 0652905), the US Office of Naval Research (Nos. N0014-019-1-0943 and N00014-09-7581-0943), Nebraska Research Initiative, Nebraska Center for Energy Sciences Research, and the National Natural Science Foundation of China (Grant No. 90923039). The authors are grateful to Drs. You Zhou, Natale Joseph Ianno and Lanping Yue, for technical support and valuable discussion. We would also like to heartily express our thanks to Joel Brehm from the University of Nebraska-Lincoln Office of Research for his high-quality graphic design work.

References

1. Wiederrecht G. Handbook of Nanofabrication. Boston, MA: Elsevier, 2009
2. Quake S R, Scherer A. From micro- to nanofabrication with soft materials. Science, 2000, 290(5496): 1536–1540
3. Henzie J, Lee J, Lee M H, Hasan W, Odom T W. Nanofabrication of plasmonic structures. Annual Review of Physical Chemistry, 2009, 60(1): 147–165
4. Zhang G Q, van Roosmalen A J. The changing landscape of micro/nanoelectronics. In: More than Moore: Creating High Value Micro/Nanoelectronics Systems. New York: Springer US, 2009, 1–31
5. Zhang G Q, VanRoosmalen A J. More than Moore: Creating High Value Micro/Nanoelectronics Systems. New York: Springer US, 2009
6. Liang J, Chen Y, Xu Y, Liu Z, Zhang L, Zhao X, Zhang X, Tian J, Huang Y, Ma Y, Li F. Toward all-carbon electronics: fabrication of graphene-based flexible electronic circuits and memory cards using maskless laser direct writing. ACS Applied Materials & Interfaces, 2010, 2(11): 3310–3317
7. Meixner A J. Nanophotonics, nano-optics and nanospectroscopy. Beilstein Journal of Nanotechnology, 2011, 2: 499–500
8. Vasa P, Ropers C, Pomraenke R, Lienau C. Ultra-fast nano-optics. Laser & Photonics Reviews. 2009, 3(6): 483–507
9. Stockman M. Light-emitting devices: from nano-optics to street lights. Nature Materials, 2004, 3(7): 423–424
10. Koch S W, Knorr A. Applied physics. Optics in the nano-world. Science, 2001, 293(5538): 2217–2218
11. Fara L, Yamaguchi M. Advanced Solar Cell Materials, Technology, Modeling and Simulation. Hershey, PA: Engineering Science Reference, 2013
12. Rau U, Abou-Ras D, Kirchartz T. Advanced Characterization Techniques for Thin Film Solar Cells. Weinheim, Germany: Wiley-VCH, 2011
13. Zaghloul U, Papaioannou G, Bhushan B, Coccetti F, Pons P, Plana R. On the reliability of electrostatic NEMS/MEMS devices: review of present knowledge on the dielectric charging and stiction failure mechanisms and novel characterization methodologies. Microelectronics and Reliability, 2011, 51(9–11): 1810–1818
14. Roncaglia A, Ferri M. Thermoelectric materials in MEMS and NEMS: a review. Science of Advanced Materials, 2011, 3(3): 401–419
15. Kumar S, Cola B A, Jackson R, Graham S. A review of carbon nanotube ensembles as flexible electronics and advanced packaging materials. Journal of Electronic Packaging, 2011, 133(2): 020906
16. Palacios T. Graphene electronics: thinking outside the silicon box. Nature Nanotechnology, 2011, 6(8): 464–465
17. Sinitskii A, Tour J M. Graphene electronics, unzipped. IEEE Spectrum, 2010, 47(11): 28–33
18. Geim A K, Novoselov K S. The rise of graphene. Nature Materials, 2007, 6(3): 183–191
19. Danilevičius P, Rekstyte S, Balciunas E, Kraniauskas A, Širmenis R, Baltriukienė D, Bukelskienė V, Gadonas R, Sirvydis V, Piskarskas A, Malinauskas M. Laser 3D micro/nanofabrication of polymers for tissue engineering applications. Optics & Laser Technology, 2013, 45: 518–524
20. Zhang Y L, Chen Q D, Xia H, Sun H B. Designable 3D nanofabrication by femtosecond laser direct writing. Nano Today, 2010, 5(5): 435–448
21. Porro S, Musso S, Giorcelli M, Chiodoni A, Tagliaferro A. Optimization of a thermal-CVD system for carbon nanotube growth. Physica E, Low-Dimensional Systems and Nanostructures, 2007, 37(1–2): 16–20
22. Shi F, Wang Y, Xue C. Synthesis of GaN nanowires by CVD method: effect of reaction temperature. Journal of Experimental Nanoscience, 2011, 6(3): 238–247
23. Bae S, Kim H, Lee Y, Xu X, Park J S, Zheng Y, Balakrishnan J, Lei T, Kim H R, Song Y I, Kim Y J, Kim K S, Özyilmaz B, Ahn J H, Hong B H, Iijima S. Roll-to-roll production of 30-inch graphene films for transparent electrodes. Nature Nanotechnology, 2010, 5(8): 574–578
24. Reina A, Jia X, Ho J, Nezich D, Son H, Bulovic V, Dresselhaus M S, Kong J. Large area, few-layer graphene films on arbitrary substrates by chemical vapor deposition. Nano Letters, 2009, 9(1): 30–35
25. Hong J, Jang J. Micropatterning of graphene sheets: recent advances in techniques and applications. Journal of Materials Chemistry, 2012, 22(17): 8179–8191
26. Xiong W, Zhou Y S, He X N, Gao Y, Mahjouri-Samani M, Jiang L, Baldacchini T, Lu Y F. Simultaneous additive and subtractive three-dimensional nanofabrication using integrated two-photon polymerization and multiphoton ablation. Light Science & Applications, 2012, 1(4): e6
27. Shi J, Lu Y F, Wang H, Yi K J, Lin Y S, Zhang R, Liou S H. Synthesis of suspended carbon nanotubes on silicon inverse-opal structures by laser-assisted chemical vapour deposition. Nanotechnology, 2006, 17(15): 3822–3826
28. Xie Z, Zhou Y, He X, Gao Y, Park J, Ling H, Jiang L, Lu Y. Fast growth of diamond crystals in open air by combustion synthesis with resonant laser energy coupling. Crystal Growth & Design, 2010, 10(4): 1762–1766
29. Park J B, Jeong M S, Jeong S H. Direct writing of carbon nanotube patterns by laser-induced chemical vapor deposition on a transparent substrate. Applied Surface Science, 2009, 255(8): 4526–4530
30. Xiong W, Zhou Y S, Mahjouri-Samani M, Yang W Q, Yi K J, He X N, Liou S H, Lu Y F. Self-aligned growth of single-walled carbon

nanotubes using optical near-field effects. Nanotechnology, 2009, 20(2): 025601
31. Odom T W, Huang J, Kim P, Lieber C M. Atomic structure and electronic properties of single-walled carbon nanotubes. Nature, 1998, 391(6662): 62–64
32. Burghard M, Klauk H, Kern K. Carbon-based field-effect transistors for nanoelectronics. Advanced Materials, 2009, 21 (25–26): 2586–2600
33. Bachtold A, Hadley P, Nakanishi T, Dekker C. Logic circuits with carbon nanotube transistors. Science, 2001, 294(5545): 1317–1320
34. Dai H. Carbon nanotubes: opportunities and challenges. Surface Science, 2002, 500(1–3): 218–241
35. Avouris P, Chen J. Nanotube electronics and optoelectronics. Materials Today, 2006, 9(10): 46–54
36. Kong J, Soh H T, Cassell A M, Quate C F, Dai H. Synthesis of individual single-walled carbon nanotubes on patterned silicon wafers. Nature, 1998, 395(6705): 878–881
37. Li Y, Mann D, Rolandi M, Kim W, Ural A, Hung S, Javey A, Cao J, Wang D, Yenilmez E, Wang Q, Gibbons J F, Nishi Y, Dai H. Preferential growth of semiconducting single-walled carbon nanotubes by a plasma enhanced CVD method. Nano Letters, 2004, 4(2): 317–321
38. Shi J, Lu Y F, Yi K J, Lin Y S, Liou S H, Hou J B, Wang X W. Direct synthesis of single-walled carbon nanotubes bridging metal electrodes by laser-assisted chemical vapor deposition. Applied Physics Letters, 2006, 89(8): 083105
39. Thess A, Lee R, Nikolaev P, Dai H, Petit P, Robert J, Xu C, Lee Y H, Kim S G, Rinzler A G, Colbert D T, Scuseria G E, Tomanek D, Fischer J E, Smalley R E. Crystalline ropes of metallic carbon nanotubes. Science, 1996, 273(5274): 483–487
40. Bethune D S, Kiang C H, de Vries M S, Gorman G, Savoy R, Vazquez J, Beyers R. Cobalt-catalyzed growth of carbon nanotubes with single-atomic-layerwalls. Nature, 1993, 363(6430): 605–607
41. Kim P, Shi L, Majumdar A, McEuen P L. Mesoscopic thermal transport and energy dissipation in carbon nanotubes. Physica B, Condensed Matter, 2002, 323(1–4): 67–70
42. Ural A, Li Y, Dai H. Electric-field-aligned growth of single-walled carbon nanotubes on surfaces. Applied Physics Letters, 2002, 81 (18): 3464–3466
43. Falvo M R, Clary G J, Taylor R M 2nd, Chi V, Brooks F P Jr, Washburn S, Superfine R. Bending and buckling of carbon nanotubes under large strain. Nature, 1997, 389(6651): 582–584
44. Vijayaraghavan A, Blatt S, Weissenberger D, Oron-Carl M, Hennrich F, Gerthsen D, Hahn H, Krupke R. Ultra-large-scale directed assembly of single-walled carbon nanotube devices. Nano Letters, 2007, 7(6): 1556–1560
45. Rao S G, Huang L, Setyawan W, Hong S. Nanotube electronics: large-scale assembly of carbon nanotubes. Nature, 2003, 425 (6953): 36–37
46. Zhang Y, Chang A, Cao J, Wang Q, Kim W, Li Y, Morris N, Yenilmez E, Kong J, Dai H. Electric-field-directed growth of aligned single-walled carbon nanotubes. Applied Physics Letters, 2001, 79(19): 3155–3157
47. Huang S, Cai X, Liu J. Growth of millimeter-long and horizontally aligned single-walled carbon nanotubes on flat substrates. Journal of the American Chemical Society, 2003, 125(19): 5636–5637
48. Tans S J, Devoret M H, Dai H, Thess A, Smalley R E, Geerligs L J, Dekker C. Individual single-wall carbon nanotubes as quantum wires. Nature, 1997, 386(6624): 474–477
49. Xi N, Szu H, Buss J, Mack I. Carbon nanotube based spectrum infrared detectors. In: Proceedings of SPIE 5987, Electro-Optical and Infrared Systems: Technology and Applications II. 2005, 59870M
50. Bockrath M, Cobden D H, McEuen P L, Chopra N G, Zettl A, Thess A, Smalley R E. Single-electron transport in ropes of carbon nanotubes. Science, 1997, 275(5308): 1922–1925
51. Maehashi K, Ohno Y, Inoue K, Matsumoto K. Laser-resonance chirality selection in single-walled carbon nanotubes. AIP Conference Proceedings, 2005, 772(1): 1023–1024
52. Xiong W, Gao Y, Mahjouri-Samani M, Zhou Y S, Mitchell M, J BPark, Lu Y F. Laser assisted fabrication for controlled single-walled carbon nanotube synthesis and processing. Chinese Journal of Lasers, 2009, 36(12): 3125–3132
53. Hayazawa N, Yano T, Watanabe H, Inouye Y, Kawata S. Detection of an individual single-wall carbon nanotube by tip-enhanced near-field Raman spectroscopy. Chemical Physics Letters, 2003, 376(1–2): 174–180
54. Novotny L, Bian R X, Xie X S. Theory of nanometric optical tweezers. Physical Review Letters, 1997, 79(4): 645–648
55. Downes A, Salter D, Elfick A. Heating effects in tip-enhanced optical microscopy. Optics Express, 2006, 14(12): 5216–5222
56. Yao Y, Li Q, Zhang J, Liu R, Jiao L, Zhu Y T, Liu Z. Temperature-mediated growth of single-walled carbon-nanotube intramolecular junctions. Nature Materials, 2007, 6(4): 283–286
57. Zhou Y S, Xiong W, Gao Y, Mahjouri-Samani M, Mitchell M, Jiang L, Lu Y F. Towards carbon-nanotube integrated devices: optically controlled parallel integration of single-walled carbon nanotubes. Nanotechnology, 2010, 21(31): 315601
58. Xiong W, Zhou Y S, Mahjouri-Samani M, Yang W Q, Yi K J, He X N, Lu Y F. Controlled-growth of single-walled carbon nanotubes using optical near-field effects. In: Proceedings of SPIE 7202, Laser-based Micro- and Nanopackaging and Assembly III. 2009, 720209
59. Cantoro M, Hofmann S, Pisana S, Scardaci V, Parvez A, Ducati C, Ferrari A C, Blackburn A M, Wang K Y, Robertson J. Catalytic chemical vapor deposition of single-wall carbon nanotubes at low temperatures. Nano Letters, 2006, 6(6): 1107–1112
60. van Dorp W F, Hagen C W. A critical literature review of focused electron beam induced deposition. Journal of Applied Physics, 2008, 104(8): 081301
61. Brintlinger T, Chen Y, Dürkop T, Cobas E, Fuhrer M S, Barry J D, Melngailis J. Rapid imaging of nanotubes on insulating substrates. Applied Physics Letters, 2002, 81(13): 2454–2456
62. Zhou Y S, Yi K J, Mahjouri-Samani M, Xiong W, Lu Y F, Liou S H. Image contrast enhancement in field-emission scanning electron microscopy of single-walled carbon nanotubes. Applied Surface Science, 2009, 255(7): 4341–4346
63. Homma Y, Suzuki S, Kobayashi Y, Nagase M, Takagi D. Mechanism of bright selective imaging of single-walled carbon nanotubes on insulators by scanning electron microscopy. Applied Physics Letters, 2004, 84(10): 1750–1752
64. Novoselov K S, Geim A K, Morozov S V, Jiang D, Katsnelson M

I, Grigorieva I V, Dubonos S V, Firsov A A. Two-dimensional gas of massless Dirac fermions in graphene. Nature, 2005, 438(7065): 197–200

65. Novoselov K S, Jiang Z, Zhang Y, Morozov S V, Stormer H L, Zeitler U, Maan J C, Boebinger G S, Kim P, Geim A K. Room-temperature quantum Hall effect in graphene. Science, 2007, 315 (5817): 1379
66. Lee C, Wei X, Kysar J W, Hone J. Measurement of the elastic properties and intrinsic strength of monolayer graphene. Science, 2008, 321(5887): 385–388
67. Seol J H, Jo I, Moore A L, Lindsay L, Aitken Z H, Pettes M T, Li X, Yao Z, Huang R, Broido D, Mingo N, Ruoff R S, Shi L. Two-dimensional phonon transport in supported graphene. Science, 2010, 328(5975): 213–216
68. Vakil A, Engheta N. Transformation optics using graphene. Science, 2011, 332(6035): 1291–1294
69. Nair R R, Blake P, Grigorenko A N, Novoselov K S, Booth T J, Stauber T, Peres N M R, Geim A K. Fine structure constant defines visual transparency of graphene. Science, 2008, 320(5881): 1308
70. Li X, Zhu H, Wang K, Cao A, Wei J, Li C, Jia Y, Li Z, Li X, Wu D. Graphene-on-silicon Schottky junction solar cells. Advanced materials (Deerfield Beach, Fla.), 2010, 22(25): 2743–2748
71. Park H, Rowehl J A, Kim K K, Bulovic V, Kong J. Doped graphene electrodes for organic solar cells. Nanotechnology, 2010, 21(50): 505204
72. Feng L, Wu L, Wang J, Ren J, Miyoshi D, Sugimoto N, Qu X. Detection of a prognostic indicator in early-stage cancer using functionalized graphene-based peptide sensors. Advanced materials (Deerfield Beach, Fla.), 2012, 24(1): 125–131
73. Myung S, Solanki A, Kim C, Park J, Kim K S, Lee K. Graphene-encapsulated nanoparticle-based biosensor for the selective detection of cancer biomarkers. Advanced materials (Deerfield Beach, Fla.), 2011, 23(19): 2221–2225
74. Hwang J O, Park J S, Choi D S, Kim J Y, Lee S H, Lee K E, Kim Y H, Song M H, Yoo S, Kim S O. Workfunction-tunable, N-doped reduced graphene transparent electrodes for high-performance polymer light-emitting diodes. ACS Nano, 2012, 6(1): 159–167
75. Hecht D S, Hu L, Irvin G. Emerging transparent electrodes based on thin films of carbon nanotubes, graphene, and metallic nanostructures. Advanced materials (Deerfield Beach, Fla.), 2011, 23(13): 1482–1513
76. Kalita G, Matsushima M, Uchida H, Wakita K, Umeno M. Graphene constructed carbon thin films as transparent electrodes for solar cell applications. Journal of Materials Chemistry, 2010, 20 (43): 9713–9717
77. Xiong W, Zhou Y S, Jiang L J, Sarkar A, Mahjouri-Samani M, Xie Z Q, Gao Y, Ianno N J, Jiang L, Lu Y F. Single-step formation of graphene on dielectric surfaces. Advanced materials (Deerfield Beach, Fla.), 2013, 25(4): 630–634
78. Wei Z, Wang D, Kim S, Kim S Y, Hu Y, Yakes M K, Laracuente A R, Dai Z, Marder S R, Berger C, King W P, de Heer W A, Sheehan P E, Riedo E. Nanoscale tunable reduction of graphene oxide for graphene electronics. Science, 2010, 328(5984): 1373–1376
79. Zhang Y, Guo L, Wei S, He Y, Xia H, Chen Q, Sun H, Xiao F. Direct imprinting of microcircuits on graphene oxides film by femtosecond laser reduction. Nano Today, 2010, 5(1): 15–20
80. Zhou Y, Bao Q, Varghese B, Tang L A L, Tan C K, Sow C, Loh K P. Microstructuring of graphene oxide nanosheets using direct laser writing. Advanced materials (Deerfield Beach, Fla.), 2010, 22 (1): 67–71
81. Park J B, Xiong W, Gao Y, Qian M, Xie Z Q, Mitchell M, Zhou Y S, Han G H, Jiang L, Lu Y F. Fast growth of graphene patterns by laser direct writing. Applied Physics Letters, 2011, 98(12): 123109
82. Park J B, Xiong W, Xie Z Q, Gao Y, Qian M, Mitchell M, Mahjouri-Samani M, Zhou Y S, Jiang L, Lu Y F. Transparent interconnections formed by rapid single-step fabrication of graphene patterns. Applied Physics Letters, 2011, 99(5): 053103
83. Xiong W, Zhou Y S, Hou W J, Jiang L J, Gao Y, Fan L S, Jiang L, Silvain J F, Lu Y F. Direct writing of graphene patterns on insulating substrates under ambient conditions. Scientific Reports, 2014, 4: 4892
84. Ferrari A C, Meyer J C, Scardaci V, Casiraghi C, Lazzeri M, Mauri F, Piscanec S, Jiang D, Novoselov K S, Roth S, Geim A K. Raman spectrum of graphene and graphene layers. Physical Review Letters, 2006, 97(18): 187401
85. Casiraghi C, Hartschuh A, Qian H, Piscanec S, Georgi C, Fasoli A, Novoselov K S, Basko D M, Ferrari A C. Raman spectroscopy of graphene edges. Nano Letters, 2009, 9(4): 1433–1441
86. Kuzmenko A B, van Heumen E, Carbone F, van der Marel D. Universal optical conductance of graphite. Physical Review Letters, 2008, 100(11): 117401
87. Rigo V A, Martins T B, da Silva A J R, Fazzio A, Miwa R H. Electronic, structural, and transport properties of Ni-doped graphene nanoribbons. Physical Review B: Condensed Matter and Materials Physics, 2009, 79(7): 075435
88. Giovannetti G, Khomyakov P A, Brocks G, Karpan V M, van den Brink J, Kelly P J. Doping graphene with metal contacts. Physical Review Letters, 2008, 101(2): 026803
89. David J M, Buehler M G. A numerical analysis of various cross sheet resistor test structures. Solid-State Electronics, 1977, 20(6): 539–543
90. Fang T, Konar A, Xing H, Jena D. Carrier statistics and quantum capacitance of graphene sheets and ribbons. Applied Physics Letters, 2007, 91(9): 092109
91. Li X, Cai W, An J, Kim S, Nah J, Yang D, Piner R, Velamakanni A, Jung I, Tutuc E, Banerjee S K, Colombo L, Ruoff R S. Large-area synthesis of high-quality and uniform graphene films on copper foils. Science, 2009, 324(5932): 1312–1314
92. Gómez-Navarro C, Weitz R T, Bittner A M, Scolari M, Mews A, Burghard M, Kern K. Electronic transport properties of individual chemically reduced graphene oxide sheets. Nano Letters, 2007, 7 (11): 3499–3503
93. Eda G, Ball J, Mattevi C, Acik M, Artiglia L, Granozzi G, Chabal Y, Anthopoulos T D, Chhowalla M. Partially oxidized graphene as a precursor to graphene. Journal of Materials Chemistry, 2011, 21 (30): 11217–11223
94. Guo L, Zhang Y, Han D, Jiang H, Wang D, Li X, Xia H, Feng J, Chen Q, Sun H. Laser-mediated programmable N doping and simultaneous reduction of graphene oxides. Advanced Optical Materials, 2014, 2(2): 120–125
95. Gates B D, Xu Q, Love J C, Wolfe D B, Whitesides G M. Unconventional nanofabrication. Annual Review of Materials

Research, 2004, 34(1): 339–372
96. Gates B D, Xu Q, Stewart M, Ryan D, Willson C G, Whitesides G M. New approaches to nanofabrication: molding, printing, and other techniques. Chemical Reviews, 2005, 105(4): 1171–1196
97. Dixon C J, Curtines O W. Nanotechnology: Nanofabrication, Patterning, and Self Assembly. New York: Nova Science Publishers Inc., 2009
98. Mailly D. Nanofabrication techniques. European Physical Journal. Special Topics, 2009, 172(1): 333–342
99. Wiley B J, Qin D, Xia Y. Nanofabrication at high throughput and low cost. ACS Nano, 2010, 4(7): 3554–3559
100. Marrian C R K, Dobisz E A, Glembocki O J. Nanofabrication – how small can devices get. R & D Magazine, 1992, 34(2): 123
101. Marrian C R K, Tennant D M. Nanofabrication. Journal of Vacuum Science & Technology. A, Vacuum, Surfaces, and Films, 2003, 21 (5): S207–S215
102. Gattass R R, Mazur E. Femtosecond laser micromachining in transparent materials. Nature Photonics, 2008, 2(4): 219–225
103. Li L, Fourkas J T. Multiphoton polymerization. Materials Today, 2007, 10(6): 30–37
104. Park S H, Yang D Y, Lee K S. Two-photon stereolithography for realizing ultraprecise three-dimensional nano/microdevices. Laser & Photonics Reviews, 2009, 3(1–2): 1–11
105. Lee K, Yang D, Park S H, Kim R H. Recent developments in the use of two-photon polymerization in precise 2D and 3D microfabrications. Polymers for Advanced Technologies, 2006, 17(2): 72–82
106. Chong T C, Hong M H, Shi L P. Laser precision engineering: from microfabrication to nanoprocessing. Laser & Photonics Reviews, 2010, 4(1): 123–143
107. Hell S W, Wichmann J. Breaking the diffraction resolution limit by stimulated emission: stimulated-emission-depletion fluorescence microscopy. Optics Letters, 1994, 19(11): 780–782
108. Feigel A, Veinger M, Sfez B, Arsh A, Klebanov M, Lyubin V. Three-dimensional simple cubic woodpile photonic crystals made from chalcogenide glasses. Applied Physics Letters, 2003, 83(22): 4480–4482
109. Gomez D, Goenaga I, Lizuain I, Ozaita M. Femtosecond laser ablation for microfluidics. Optical Engineering (Redondo Beach, Calif.), 2005, 44(5): 051105
110. Korte F, Serbin J, Koch J, Egbert A, Fallnich C, Ostendorf A, Chichkov B N. Towards nanostructuring with femtosecond laser pulses. Applied Physics. A, Materials Science & Processing, 2003, 77(2): 229–235
111. Suriano R, Kuznetsov A, Eaton S M, Kiyan R, Cerullo G, Osellame R, Chichkov B N, Levi M, Turri S. Femtosecond laser ablation of polymeric substrates for the fabrication of microfluidic channels. Applied Surface Science, 2011, 257(14): 6243–6250
112. Chichkov B N, Momma C, Nolte S, Von Alvensleben F, Tünnermann A. Femtosecond, picosecond and nanosecond laser ablation of solids. Applied Physics. A, Materials Science & Processing, 1996, 63(2): 109–115
113. Sun H B, Xu Y, Juodkazis S, Sun K, Watanabe M, Matsuo S, Misawa H, Nishii J. Arbitrary-lattice photonic crystals created by multiphoton microfabrication. Optics Letters, 2001, 26(6): 325–327
114. Zhou G, Gu M. Direct optical fabrication of three-dimensional photonic crystals in a high refractive index $LiNbO_3$ crystal. Optics Letters, 2006, 31(18): 2783–2785
115. Gu M, Jia B, Li J, Ventura M J. Fabrication of three-dimensional photonic crystals in quantum-dot-based materials. Laser & Photonics Reviews, 2010, 4(3): 414–431
116. Fischer P, McWilliam A, Paterson L, Brown C T A, Sibbett W, Dholakia K, MacDonald M P. Two-photon ablation with 1278 nm laser radiation. Journal of Optics. A, Pure and Applied Optics, 2007, 9(6): S19–S23
117. Waldbaur A, Rapp H, Länge K, Rapp B E. Let there be chip-towards rapid prototyping of microfluidic devices: one-step manufacturing processes. Analytical Methods, 2011, 3(12): 2681–2716
118. Goldman J R, Prybyla J A. Ultrafast dynamics of laser-excited electron distributions in silicon. Physical Review Letters, 1994, 72 (9): 1364–1367
119. Xiong W, Zhou Y S, He X N, Gao Y, Mahjouri-Samani M, Baldacchini T, Lu Y F. Three-dimensional sub-wavelength fabrication by integration of additive and subtractive femtosecond-laser direct writing. In: Proceedings of MRS, Volume 1499, 2013
120. Zappe H P. Fundamentals of Micro-Optics. Cambridge, New York: Cambridge University Press, 2010
121. Qin D, Xia Y, Whitesides G M. Soft lithography for micro- and nanoscale patterning. Nature Protocols, 2010, 5(3): 491–502

Wei Xiong is currently a postdoctoral research associate in Laser Assisted Nano Engineering (LANE) Lab at University of Nebraska-Lincoln (UNL). He received his Ph.D. degree in electrical engineering from University of Nebraska-Lincoln in 2013 and obtained his B.Sc. and M.Sc. degrees from Huazhong University of Science and Technology in 2004 and Fudan University in 2007, respectively. His research interests include synthesis and integration of carbon nano-materials such as carbon nanotubes and graphene, and 3D fabrication of polymeric and carbon-based functional micro/nano-structures. Currently he is working on 3D micro/nanofabrication and large-scale 2D material synthesis.

Yongfeng Lu is currently the Lott Distinguished Professor of Engineering at the University of Nebraska-Lincoln (UNL). He received his bachelor degree from Tsinghua University (China) in 1984 and M.Sc. and Ph.D. degrees from Osaka University (Japan) in 1988 and 1991, all in electrical engineering. From 1991 to 2002, he was a faculty in the ECE Department at National University of Singapore. He joined the Department of Electrical Engineering at UNL in 2002. He has more than 20 years of experience in processing and characterization of micro/nanostructured materials. His group has research projects funded by NSF,

AFOSR, ONR, DTRA, DOE, DOT, NCESR, NRI, private companies, and other foundations in Japan, with research expenditures of $20 million in the past a few years. His research has led to a number of commercialization and product developments. Dr. Lu has authored or co-authored over 300 journal papers and 350 conference papers. He has been elected to SPIE fellow, LIA fellow, and OSA fellow. He served as the President of the Laser Institute of America in 2014. He has also served as chair and general chair for major international conferences in the field including the general congress chair for the International Congress of Applications of Lasers and Electro-Optics in 2007 and 2008, and general co-chair for LASE in Photonics West 2014 and 2015.